

APPLIED SCIENCES AND ENGINEERING

A miniaturized implantable electrochemical platform for continuous monitoring of metabolites in deep tissue

Kenneth E. Madsen^{1,2*}, Dane Hintermueller¹, Elliot A. Opel³, Joseph G. Ribaldo⁴, Sara Saffari⁴, Soongwon Cho¹, Joanna L. Ciatti^{1,5}, Yu-Ting Huang^{1,6}, Amanda M. Westman⁴, Ralph G. Nuzzo^{2,7}, Mitchell A. Pet^{4*}, John A. Rogers^{1,3,5,6,8,9*}

The loss or suppression of local metabolic function in living tissues brought about by a lack of oxygen availability (ischemia) serves as the origin for myriad life-threatening conditions including stroke, heart failure, and peripheral ischemic injury. Despite the pressing clinical need to evaluate local tissue health, platforms that support such analysis remain elusive. To address this need, we present a wireless, minimally invasive, multianalyte, electrochemical probe supporting the continuous profiling of local metabolites including K^+ and pH, and the semicontinuous profiling of lactic acid. We validate the analytical capabilities of our sensing system by ion profiling in arterial whole blood. Furthermore, we use acute compartment syndrome as a model for tissue ischemia and use our percutaneously implanted probes to track metabolic changes in living muscle in real time.

INTRODUCTION

Disruptions to local tissue metabolism induced by insufficiencies in oxygen supply remain among the most common and detrimental etiologies of mortality in the developed world (1). The consequences of prolonged disruptions to normal cellular respiration brought about by a reduction or total loss of tissue perfusion (ischemia) are apparent in numerous pathologies including ischemic stroke, myocardial infarction, mesenteric ischemia, chronic limb threatening ischemia, and acute compartment syndrome (ACS) among many others (2–6). The potential severity of ischemic insult makes the prompt detection of metabolic changes in target tissues imperative to affect successful clinical intervention before the onset of irreversible damage.

The need for prompt clinical intervention is apparent in cases of ACS, wherein ischemia, localized to a muscle compartment (stemming from direct trauma or ischemia/reperfusion), induces tissue swelling and a concomitant increase in compartment pressure (Fig. 1A). With no avenue for pressure relief, this swelling can result in the compression of the venous system draining the compartment, reinforcing a positive feedback loop that exacerbates swelling and further increases compartment pressure resulting in tissue necrosis. Current clinical reports suggest that the onset of ACS generally occurs within 12 to 24 hours of initial trauma, with some cases proceeding within 2 to 3 hours. Similarly, if ACS is allowed to progress without timely intervention (within 4 hours), irreversible tissue necrosis of the affected area is very likely (7). At present, the only clinical remediation available for ACS is a surgical fasciotomy to return the compartment to normal pressure/perfusion (8–10). While surgical fasciotomies are effective at restoring

normal tissue perfusion, they are accompanied by extended hospital stays, increased treatment cost, infection, and cosmetic issues. Furthermore, failure to recognize ACS as it onsets is among the most heavily litigated issues in interventional medicine (11–14). To this end, technologies capable of monitoring tissue perfusion and metabolic health in real time could be invaluable in the prophylactic treatment of local oxygen deficiencies or in the early detection of ACS to minimize the severity of tissue damage (15).

Existing technologies to quantify the onset of ACS primarily rely on direct measurement of compartment pressure using either single-point (16) or continuous recording apparatus (17, 18). Other work has aimed to use blood flow (19, 20) or tissue oxygen saturation (StO_2) (21) to evaluate tissue perfusion to provide an early diagnosis of tissue distress. Last, implantable electrochemical biosensors have been demonstrated to directly monitor the chemical onset of metabolic disruptions associated with ischemia. Implantable lactate (22–24), potassium (25, 26), oxygen (27–29), and pH (30, 31) probes have seen successful deployment in blood (23, 25, 26, 29) and muscle (28, 30, 31), making electrochemical detection an attractive approach to track metabolic changes proximal to sensing electrodes. Unfortunately, most of these demonstrations only support single-analyte quantification and rely on comparatively bulky recording apparatus, limiting the versatility and convenience of these sensing systems.

Here, we report the development of a robust, minimally invasive, multianalyte electrochemical probe facilitating the continuous quantification of tissue potassium and pH, and the semicontinuous profiling of lactate as universal byproducts of anaerobic cellular respiration (Fig. 1B). While numerous other biomarkers can be used for similar profiling (glucose, O_2 , and creatine kinase), we focus on these targets due to the comparative maturity of electrochemical strategies for their detection and their prevalence in existing literature describing the biochemical presentation of ACS. Contrasting alternative methods to evaluate tissue distress, electrochemical methods offer direct and absolute quantification of local metabolites, providing a rich body of information to characterize the onset of metabolic insufficiencies regardless of origin. Electrochemical reporters are independent of blood pressure or other hemodynamic considerations, making them a more direct method to evaluate tissue health and viability. Similarly, the ability to profile multiple analytes (metabolites and ions)

¹Querrey Simpson Institute for Bioelectronics, Northwestern University, Evanston, IL 60208, USA. ²Department of Chemistry, University of Illinois at Urbana-Champaign, Urbana, IL 61801, USA. ³Department of Biomedical Engineering, Northwestern University, Evanston, IL 60208, USA. ⁴Division of Plastic and Reconstructive Surgery, Washington University School of Medicine, St Louis, MO 63110, USA. ⁵Department of Materials Science and Engineering, Northwestern University, Evanston, IL 60208, USA. ⁶Department of Mechanical Engineering, Northwestern University, Evanston, IL 60208, USA. ⁷Division of Surface and Corrosion Science, KTH Royal Institute of Technology, Stockholm 10044, Sweden. ⁸Department of Neurological Surgery, Feinberg School of Medicine, Northwestern University, Chicago, IL 60611, USA. ⁹Department of Chemistry, Northwestern University, Evanston, IL 60208, USA.

*Corresponding author. Email: kenneth.madsen@northwestern.edu (K.E.M.); mpet@wustl.edu (M.A.P.); jrogers@northwestern.edu (J.A.R.)

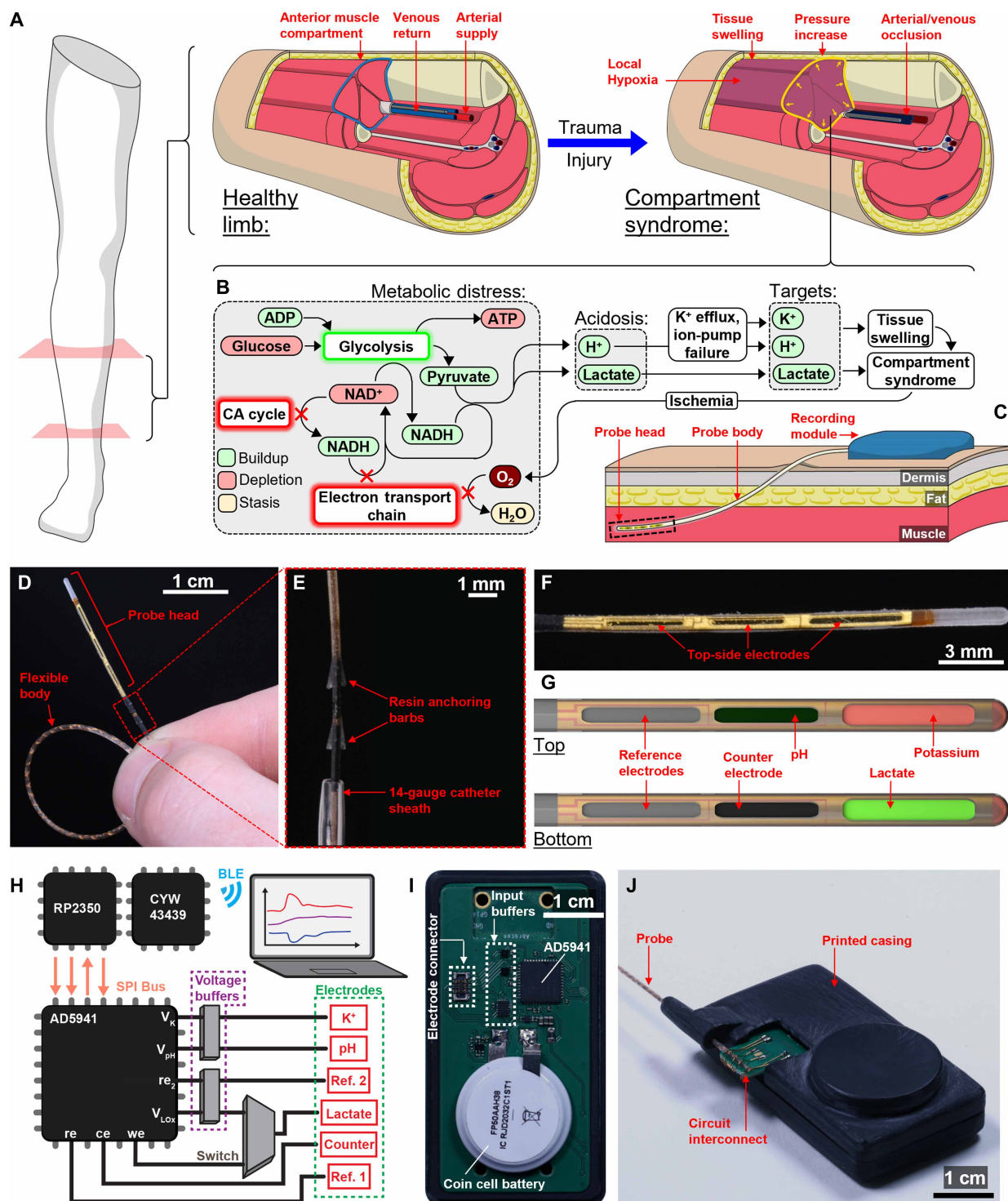


Fig. 1. Metabolite targets and electrochemical probe construction. (A) Schematic depiction of trauma induced limb compartment syndrome. (B) Anaerobic biochemical cascade induced by ischemia leading to the up-regulation of glycolysis and generation of measurable deviations in local potassium, lactate, and H⁺ concentrations. (C) Operating concept for an implantable electrochemical probe to continuously measure local metabolite concentrations. (D) Photograph of a fully assembled electrochemical probe. (E) Side-on photograph taken at the base of the probe head highlighting its delivery via a 14-gauge intravenous catheter. (F) Magnified view of the probe head highlighting individual electrode pads. (G) Electrode locations facilitating continuous K⁺, pH, and lactate measurement. (H) Measurement and communication protocol. (I) Photograph of the AFE circuit supporting electrochemical data collection. (J) Photograph of the fully assembled sensing platform including a 3D-printed case housing and detachable electrochemical probe. (A), (C), and (H) were produced using Adobe Illustrator. (G) was rendered in Blender.

simultaneously provides greater confidence in the determination of tissue distress and offers the possibility to mechanically evaluate the dynamics of tissue metabolism in response to insult.

The electrochemical platform considered here consists of a single-use, multianalyte implantable probe supporting six individually addressable macroscopic (millimeter-scale) electrodes within a sufficiently small footprint (1-mm diameter) to accommodate percutaneous introduction via an intravenous catheter. Despite their small size, these electrochemical probes incorporate engineering strategies (recessed electrode wells, patterned structures for mechanical engagement with tissue, and superelastic support armatures) to improve electrode stability and signal quality in the biomechanically challenging environments encountered in living muscle tissue. Using a combination of laser patterning, soft lithography, and injection molding, this platform merges the signal multiplexing common to microelectrode arrays with the stability of macroscopic electrochemical architectures. Furthermore, the multianalyte probes described here maintain exceptional flexibility and robustness similar to the mechanical attributes associated with coated wire assemblies. Last, by coupling electrochemical probes with custom wireless recording apparatus, we demonstrate the unique capability of this electrochemical platform to profile early changes to cellular metabolism heralding the onset of severe ACS in living muscle tissue in real time. More broadly, this platform may prove amenable to other electrochemically active biomarkers, making it a versatile approach to biochemical profiling in the challenging environment of live tissue.

RESULTS

Platform design

The metabolite sensing system considered here comprises an implantable catheter-type electrochemical probe and dermally mounted recording/communication module as depicted schematically in Fig. 1C. The double-sided probe supports a total of six individually addressable electrodes with a sufficiently small footprint to accommodate percutaneous implantation through an intravenous catheter (14-gauge, 1.588-mm inner diameter). Probes are assembled in two sections: a polyimide (PI) sensing head, and a nitinol reinforced body connecting the head to the recording module. A semicylindrical resin sheath (with a maximum outer diameter of 1.4 mm; fig. S1) serves to encapsulate/protect the electrodes, yielding the flexible assembly displayed in Fig. 1D. In addition to its role as encapsulant, the sheath also serves to mechanically anchor the probe within target tissue via patterned barbs along the top and bottom surfaces of the device (Fig. 1E). The nominal top side of the device (presented photographically in Fig. 1F) contains potentiometric sensing electrodes for pH and K^+ , and a solid-contact Ag/AgCl reference electrode (Fig. 1G, top). The bottom side of the probe supports lactate sensing elements with another Ag/AgCl reference electrode, a Au counter electrode, and an enzyme-loaded, lactate sensing electrode (Fig. 1G, bottom).

Data acquisition and transmission are accomplished by means of a dedicated electrochemical analog front end (AFE) communicating via a serial peripheral interface (SPI) to a Bluetooth low-energy (BLE) system on chip (Fig. 1, H and I). The sensing system leverages the AFE's working, counter, and reference electrodes to facilitate discrete amperometric lactate profiling. Likewise, the AFE's general purpose analog inputs continuously record potentiometric data from the two cation sensing electrodes, which can then be sent wirelessly to BLE-enabled devices for real-time sensor calibration and data visualization.

Due to the single, on-chip, analog to digital converter, amperometric and potentiometric profiling cannot proceed simultaneously; thus, amperometric data are acquired at discrete time points rather than continuously. The total footprint of the recording apparatus is $3 \times 6 \text{ cm}^2$ and accommodates quick replacement of disposable electrochemical probes through a top-mounted snap connector (fully assembled system presented in Fig. 1J).

To support data streaming from the recording apparatus, communication and visualization are accomplished through a custom MATLAB script, which also enables user control over potentiostat functions. The data acquisition software provided here accommodates real-time data visualization of potentiometric and amperometric profiles. Similarly, control functions allow the user to initiate a single on-demand amperometric measurement if desired. Other functions allow for a full hardware reset of the AFE, a sensor calibration function for single-point calibration using standard solution, and an internal sensor self-test to evaluate the reliability of in vivo data. Specifically, the sensor self-test measures the voltage difference between the two reference electrodes implanted in the medium and records an error if the voltage deviation is greater than a target value (10 mV). Greater detail on software implementation and communication capabilities is provided in the Supplementary Materials.

Probe design and mechanics

Figure 2A presents an exploded-view schematic of the distal end of the electrochemical probe detailing the interconnect circuitry linking the sensing head and probe body. The probe head is assembled from laser-patterned Au electrodes supported on flexible PI film (75- μm thickness). The electrode assembly abuts a flexible printed circuit board (FPCB) onto which copper leads (outer diameter of 80 μm) are attached to facilitate data transmission. Electrical connection between traces on the probe head and to those on the FPCB is realized with two bridging circuits patterned from single-sided Au/PI film. Polyolefin heat-shrink tubing is used to align overlapping traces and form robust elastic connections between disparate components. Following the union of the probe head and body, devices are encapsulated in a semicylindrical resin sheath via injection molding (fig. S2) leaving patterned apertures (300- μm depth; fig. S3, A and B) to expose individual electrodes. This approach (detailed completely in Materials and Methods and fig. S2) permits the fabrication of probes of arbitrary length (fig. S4) with diverse encapsulation geometries to control the mechanical coupling between the probe and tissue.

Figure 2B presents height profiles from three different encapsulation geometries including a flat, textured (sinusoidal, 600- μm wavelength, 150- μm amplitude), and barbed (400- μm height, 1.5-mm length) surface topology. The mechanical interaction between these geometries and muscle tissue is quantified in Fig. 2C by force-displacement curves obtained during probe explantation from a tissue facsimile. Regardless of surface geometry, all probes display similar retaining forces at low displacement, likely associated with local tissue deformation. At larger displacements, flat and sinusoidally textured surfaces display a rapid decrease in retaining force as probes slip from their initial positions. Per contra, barbed probes exhibit a dramatic increase in force prior to slipping. The peak magnitude of this force is presented in Fig. 2D, displaying a fivefold increase in retaining force from barbed probes relative to sinusoidally textured probes, and a 10-fold increase relative to flat probes

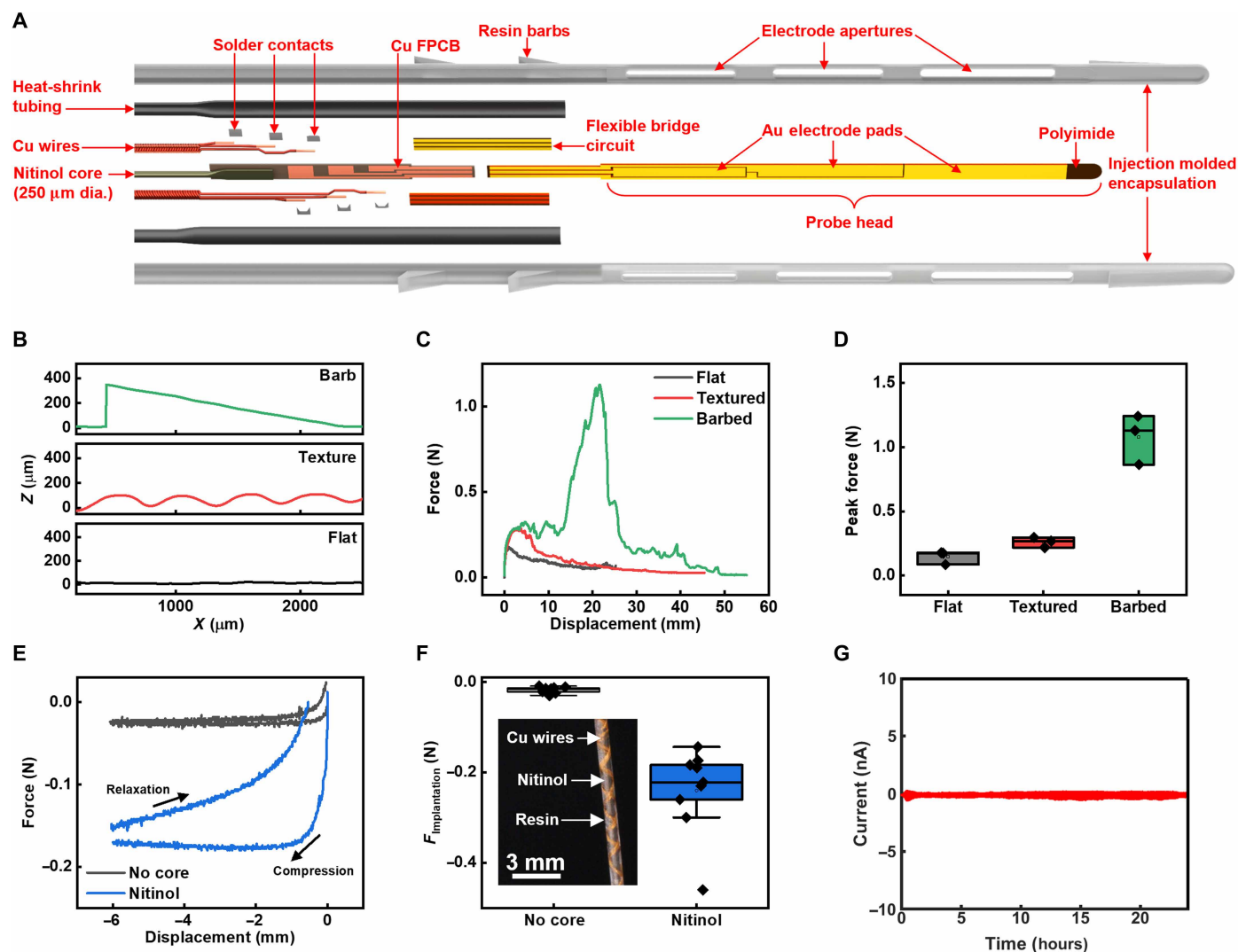


Fig. 2. Implantable probe construction and mechanical characteristics. (A) Exploded view schematic of the distal end of the implantable electrochemical probes highlighting the sensing probe head and the interconnect circuitry facilitating communication with the recording module. (B) Height profiles of different surface textures patterned along the outer surface of the probe encapsulation. (C) Simulated explantation of probes with different surface topologies from a tissue facsimile. (D) Peak force developed during explantation as a function of probe topology ($n = 3$ replicate devices; boxes, full range of values; lines, mean values). (E) Bending mechanics obtained from linear compression of implantable probes fabricated with (blue trace) and without (black trace) a nitinol support. (F) Steady-state implantation force developed during uniaxial compression of implantable probes ($n = 9$ measurements from three replicate devices; black symbols, measured values; boxes, interquartile range; horizontal lines, mean values; whiskers, 5th to 95th percentiles). (G) Leakage current obtained from an implantable probe during uniaxial cyclic compression. (A) was rendered in Blender.

indicating the positive engagement of barbs anchoring the probe within the tissue. Notably, despite the positive mechanical engagement with tissue, barbs are still sufficiently small to accommodate delivery via a catheter. This allows the retraction of probes without inducing tissue damage beyond what is already incurred on probe delivery.

While the geometry of the encapsulating sheath improves probe retention, modifications to the probe body yield similar improvements to probe implantation. To ensure reliable and stable device delivery along a catheter sheath, a nitinol core is incorporated into the probe body (inset of Fig. 2F). Figure 2E provides representative force-displacement curves obtained during uniaxial probe compression and subsequent relaxation to simulate probe implantation. Regardless of construction, devices exhibit a roughly constant force plateau during compression associated with the elastic deformation

of the probe body with modest hysteresis during relaxation due to heat dissipation and deformation losses common to viscoelastic and polymeric materials (32, 33). Notably, probes assembled with a nitinol core develop much greater forces under equivalent deformation than those without a core, indicating greater probe stiffness accompanying nitinol reinforcement. These data, consolidated in Fig. 2F, support the use of mechanical reinforcement to improve probe delivery without incurring potentially destructive device deformations. Last, Fig. 2G presents water barrier measurements of the encapsulating sheath in an aqueous environment [phosphate-buffered saline (PBS), pH 7.4] during cyclic deformation (5% compressive deformation, 0.1-Hz compression frequency). The negligible leakage current obtained over 24 hours supports the functionality of the encapsulating sheath in preventing water infiltration to probe interconnects.

Potentiometric sensor assembly and calibration

Figure 3A presents an exploded view schematic of the top side of the electrochemical probe, detailing the electrode treatments necessary to achieve potentiometric pH and K^+ quantification. Accurate cation quantification in this configuration is predicated on a stable, chemically invariant, reference potential, realized here with a solid-contact Ag/AgCl reference electrode. Figure 3B details the composition of the reference electrode, which leverages an Ag/AgCl transducing layer, a composite membrane of AgCl/Ag nanoparticles (AgNPs), and a protective layer of agarose (cross-sectional optical micrograph

displayed as inset). The electrochemical performance of the AgNP electrode is presented in Fig. 3 (C and D), compared against electrodes fabricated with membranes composed of a sulfonated fluoropolymer (Nafion; black trace) and NaCl-loaded polyvinylbutyral (PVB; red trace). Figure 3C provides the open-circuit potential of these electrodes in PBS measured against a commercial double-junction Ag/AgCl electrode. While all electrodes display stable baseline potentials, the low ionic conductivity and concomitantly high membrane impedance of PVB (300 kilohm; fig. S5) result in electrodes with unacceptably high root mean square noise (RMS = 6.82 mV,

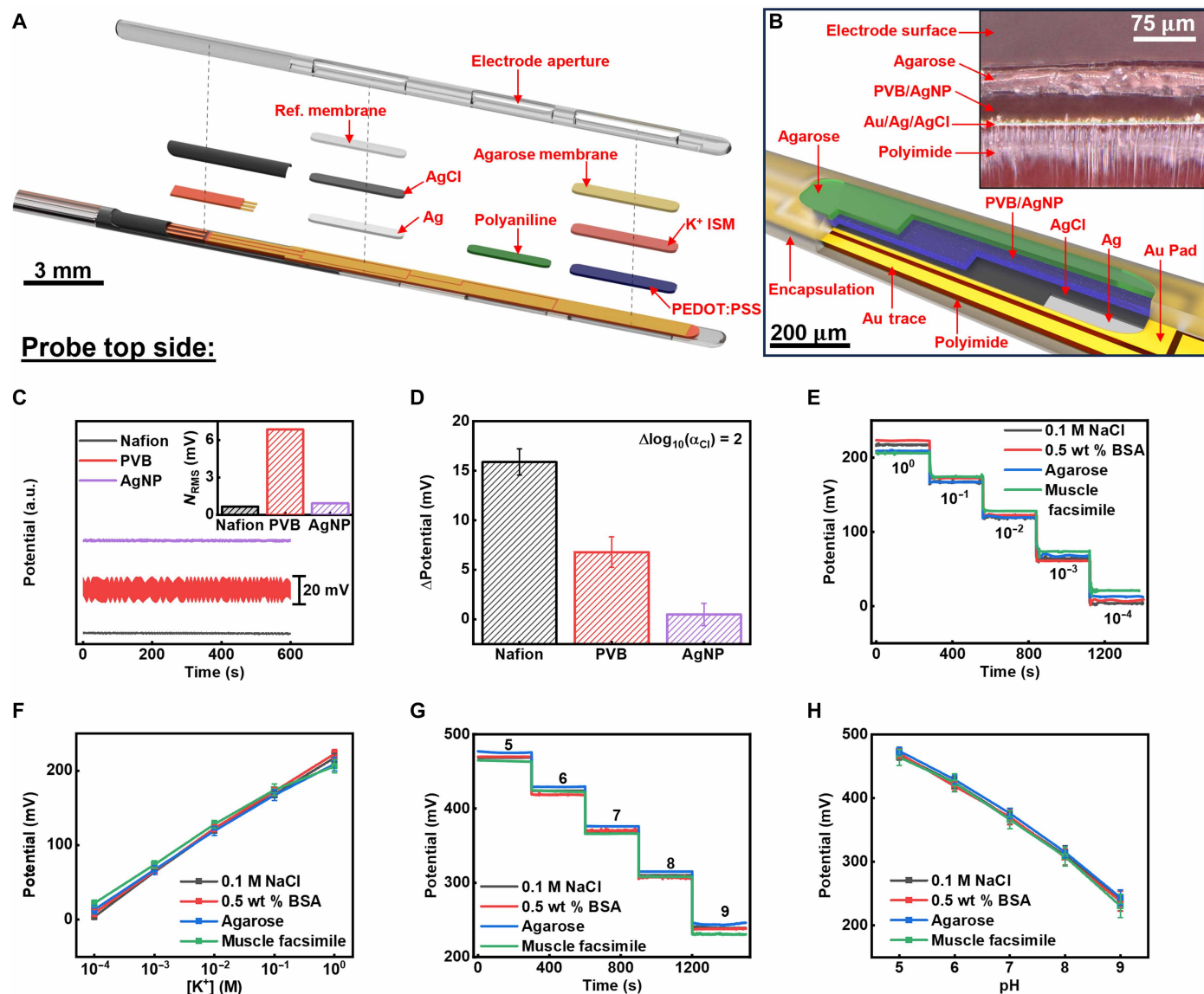


Fig. 3. Potentiometric sensing module and in vitro calibration studies. (A) Exploded view schematic of the top side of the implantable ion sensing platform highlighting potentiometric cation sensors for K^+ and pH. (B) Detailed cross-sectional schematic of reference electrode chemistry facilitating stable, chemically invariant performance in various media (inset presents a cross-sectional optical micrograph of the electrode assembly). (C) Reference potential stability compared against a commercial double junction Ag/AgCl electrode (inset provides the RMS noise displayed by different reference chemistries). (D) Reference electrode response to a 100-fold decrease in exogenous Cl^- . (E) Raw potentiometric response of the K^+ sensing electrode in different media. (F) Potentials developed at the K^+ sensing electrode at different K^+ concentrations in different fluid environments. (G) Raw potentiometric response of the pH sensing electrode in different media. (H) Potentials developed at the pH sensing electrode in different fluid environments (error bars for all measurements represent one standard deviation from the mean obtained from replicate devices; $n = 3$). (A) and (B) were rendered in Blender.

inset). This noise is markedly diminished by the inclusion of a high mass loading of AgNPs (RMS = 0.917 mV) likely due to the increased concentration and mobility of Ag^+ and Cl^- within the membrane (fig. S5).

In addition to the reduction in overall noise, AgNP solid contact electrodes demonstrate lower potentiometric deflection with changes to exogenous Cl^- activity when compared against Nafion or PVB membranes. Figure 3D displays the change in electrode potentials when subject to a 100-fold decrease in Cl^- activity (additional potentiometric data provided in fig. S5A). While Nafion and PVB membranes exhibit large potential changes (15.9 and 6.8 mV, respectively), AgNP electrodes display greater Cl^- insensitivity (0.47 mV) over the same concentration range. The Cl^- insensitivity persists even over long durations (12 hours), with reference electrodes displaying stable (<3-mV drift) potentials in both chloride-rich (150 mM) and chloride-deficient (50 mM) environments (fig. S5).

Leveraging the chemical insensitivity and potential stability of the AgNP reference electrodes, ion-selective membrane electrodes (ISEs) are used to realize selective potentiometric potassium sensing. In this configuration, potassium-sensing ion-selective membranes (ISMs) consist of a conducting film of polyethylenedioxythiophene: polystyrenesulfonate (PEDOT:PSS) coated with a valinomycin-loaded polyvinylchloride (PVC) membrane as described elsewhere (30, 34). The potassium response of each electrode is presented in Fig. 3E in a 0.1 M NaCl electrolyte, a protein-loaded NaCl solution [0.5 wt % bovine serum albumin (BSA)], an agarose gel (1 wt % agarose), and a tissue facsimile (pork loin incubated in standard calibration solution). Sensing electrodes exhibit near-Nernstian potentiometric responses to changes in local $[\text{K}^+]$ irrespective of the sampling environment (slope = 51.5 ± 2.6 mV decade $^{-1}$; Fig. 3F), confirming the suitability of this electrode architecture in quantifying local ion activity even when in direct contact with a solid or semisolid boundary. In addition to the K^+ ISM, a polyaniline (PANI) pH sensing electrode is also included to complete the cation sensing module. The pH sensor is fabricated by electrodeposition and subsequent conditioning by cyclic voltammetry in H_2SO_4 (10 mM). Figure 3G presents calibration data for pH sensing electrodes in the same solution environments used to calibrate the K^+ sensor. As detailed in Fig. 3F, PANI films display linear potentiometric responses to pH with a slope of 55.7 ± 0.7 mV decade $^{-1}$ in good agreement with a one-electron Nernstian redox couple (35).

In addition to sensitivity, sensor stability in physiological media is a critical consideration. To align with current clinical demands, sensors should be capable of extended recording times (12 hours) to monitor the metabolic health of at-risk tissues following injury. The long-term stability of potentiometric sensors both in heparinized arterial whole blood and in the same tissue facsimile used for sensor calibration is presented in fig. S6. Sensors display low drift (<3 mV) for recording durations less than 12 hours, supporting the feasibility of this electrode architecture in delivering critical biomarker data over a clinically relevant duration. Recording durations longer than 12 hours result in sufficiently large sensor drift that recalibration or replacement is necessary ($\Delta V > 5$ mV). If longer recording durations are desired, the percutaneous delivery of probes via catheter supports rapid device replacement (implantation time of ~30 s) to extend the functional recording lifetime.

Amperometric sensor assembly and calibration

Figure 4A presents an exploded view schematic of the bottom side of the electrochemical probe detailing electrode modifications necessary

to facilitate amperometric lactate quantification. The lactate module is assembled as a three-electrode cell with a lactate oxidase (LOx) working electrode, a Au counter electrode, and a second AgNP reference electrode. An enzyme-loaded chitosan membrane drop-cast on the porous gold working electrode serves to oxidize exogenous lactate to pyruvate with the concomitant reduction of O_2 to H_2O_2 . An electrocatalytic layer of Prussian blue deposited on the electrode surface reduces the resulting peroxide to H_2O , yielding a measurable reductive current correlated with the local lactate concentration (36).

Despite its activity toward peroxide reduction (37, 38), the stability of Prussian blue films under continuous reductive polarization is limited due to the aqueous solubility of Fe(II) and the progressive basification of analyte solution during peroxide reduction (39, 40). These limitations can be circumvented, however, by changing the measurement approach from continuous reduction to semicontinuous pulsed reduction as elucidated in Fig. 4B. Under this protocol, the working electrode remains inactive (allowed to relax to its open circuit potential) until time of measurement. During measurement, the working electrode is first polarized reductively (-0.2 V, 30 s) to consume locally high levels of H_2O_2 generated by LOx. Following this prerelaxation, the working electrode is allowed to return to its baseline potential during which time LOx continues to generate H_2O_2 in response to nearby lactate. Following a 30-s relaxation period, the electrode is again polarized reductively (-0.2 V, 30 s) with the current recorded during this second pulse regarded as the true measurement.

Figure 4C presents finite element simulations of the above protocol under assumptions of a diffusion-limited electrode reaction with Michaelis-Menten enzyme kinetics (details provided in fig. S7) (41). With an ambient lactate concentration of 5 mM, concentration maps of local H_2O_2 report a high steady-state value (>0.6 mM) near the electrode surface due to the continuous action of LOx. This high starting concentration decreases substantially (<0.1 mM at 30 s) during initial reductive polarization due to the electrocatalytic decomposition of H_2O_2 at the electrode/solution interface. Following the conditioning pulse, H_2O_2 concentrations begin to increase as LOx consumes exogenous lactate. Last, during the measurement pulse, the working electrode reduces the H_2O_2 generated during the recovery period, resulting in the simulated chronoamperometric traces presented in Fig. 4D. Overall, this analysis suggests that a pulsed measurement protocol is effective at removing high local H_2O_2 concentrations and standardizing the electrode environment for measurement, thereby improving the reproducibility of lactate quantification. Likewise, long-term studies (figs. S6 and S8) reveal the high stability of Prussian blue under a pulsed measurement protocol, reporting little drift even after 85 sequential measurements in 10 mM sodium lactate (total measurement duration of ~9 hours).

Figure 4E provides chronoamperograms obtained from lactate biosensors in different environments at progressively increasing lactate concentrations (only the measurement pulse is presented for clarity). Irrespective of environment, lactate probes display the characteristic Cottrellian decay expected of a diffusion-limited electrochemical reaction (35), indicating nominal device function in diverse liquid and semisolid media. Furthermore, probes display a progressive increase in the magnitude of reductive current density with increasing lactate concentration. This trend is quantified in Fig. 4F by sampling the electrode current 10 s after the onset of reduction. Probes display a linear correlation between current density and local lactate concentration within a physiologically relevant range regardless of the calibration medium. Furthermore, good reproducibility is

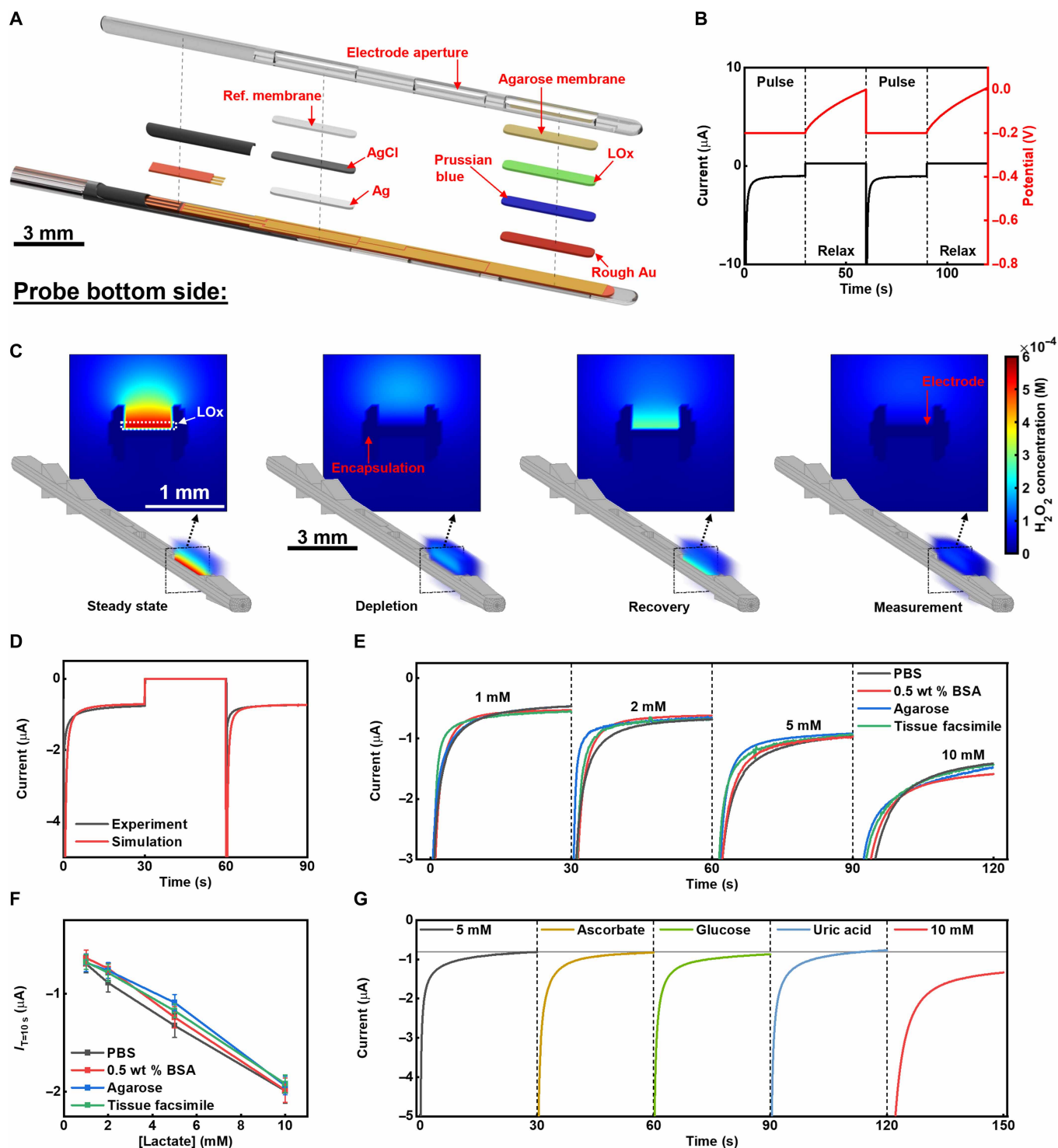


Fig. 4. Amperometric sensing module, finite element simulations, and in vitro calibration studies. (A) Exploded view schematic of the bottom side of the implantable ion sensing platform highlighting the electrode assembly facilitating amperometric lactate sensing. (B) Example pulse protocol implemented to accommodate stable amperometric data collection. (C) Finite element simulation of the pulsed protocol displayed in (B) at a 5 mM steady-state lactate concentration. Simulations depict H₂O₂ concentrations surrounding the probe at steady state (left), during prepolarization (left middle), during recovery (right middle), and during final measurement (right). (D) Comparison of experimental and simulated amperometric responses. (E) Chronoamperometric traces obtained during the measurement pulse from probes immersed in standard lactate solutions in different solution environments. (F) Reductive current values sampled 10 s into the measurement pulse correlated to the concentration of lactate (error bars represent one standard deviation from the mean; $n = 3$). (G) Chronoamperograms obtained at a lactate concentration of 5 mM in PBS with the sequential addition of 10 mM interfering species followed by concentration to 10 mM lactate (red trace). (A) was rendered in Blender.

obtained across probes when sampled using the pulsed protocol, revealing a coefficient of variance of 0.091 across three probes when measured in PBS (5 mM exogenous lactic acid).

Additional evaluation of the dynamic range of the lactate sensing module is presented in fig. S9 where unmodified lactate sensors display stable function up to ~20 mM lactate. Higher concentration ranges (up to 40 mM) can be accessed by the addition of a diffusion-limiting membrane [cellulose acetate butyrate (CAB)]; however, this was deemed unnecessary in practice, as physiological concentrations did not exceed 15 mM. Similarly, as the expected serum lactate concentration falls around 1 mM, and concentrations above 4 mM constitute lactic acidosis, unmodified probes are well capable of monitoring these levels in whole blood. In a tissue environment, local lactate can exceed these values, reaching levels above 25 mM in extreme cases of ischemia (42). In these instances, probes modified with a CAB membrane would be appropriate. Likewise, due to the multiplexed assembly of the probes considered here, it is possible to include two lactate working electrodes (one uncoated and one CAB-coated) to extend the reliable sensing range to cover even the most severe cases of tissue acidosis.

Last, Fig. 4G presents chronoamperometric data obtained from lactate sensors immersed in a 5 mM solution of sodium lactate in PBS with the addition of 10 mM of common interfering species (sodium ascorbate, glucose, and uric acid). Electrodes display negligible changes in signal in the presence of these interferents. In addition to interfering species, the long-term stability of lactate sensing electrodes is presented in fig. S6 in whole blood and a tissue facsimile. Over the course of 12 hours, little change is apparent in the amperometric response, reinforcing the capability of pulsed measurement in standardizing the electrode current response.

Ion quantification and sensor validation in arterial whole blood

The results presented in Figs. 3 and 4 demonstrate the sensitivity and selectivity of the multianalyte electrochemical probe and validate its functionality in various liquid and semisolid media. Further validation of this platform is realized by ion quantification in arterial whole blood samples collected from anesthetized swine during periods of normal oxygenation and induced hypoxia. Sequential periods of normal breathing and controlled hypoxemia are induced via control of the animals' breathing gas and monitored in real time by SpO₂ quantification. Figure 5A displays a representative deoxygenation profile with two periods of induced hypoxia. An indwelling arterial line affords continuous access to whole blood samples, and an arterial blood gas (ABG) analyzer provides ground truth chemical compositions to compare against results obtained electrochemically.

Figure 5B presents raw ABG data obtained from blood samples during a normoxic baseline (B), and during periods of hypoxia (H) and normoxemia (N) correlated against SpO₂ (purple trace). Single point concentrations of systemic lactate (black), potassium (red), pH (blue), and chloride (green) are obtained from each sample (a complete panel of chemical species detected by ABG is provided in fig. S10). Substantial changes to circulating ion concentrations are apparent in nearly all species of interest, with blood lactate, potassium, and chloride increasing during initial deoxygenation. These changes align well with previous literature on systemic deoxygenation and are characteristic of anaerobic metabolic activity (43). Notably, despite the marked increases in concentration during the initial deoxygenation cycle, subsequent cycles do not display further increases

in circulating ion concentrations. Furthermore, despite reintroduction of oxygen to the breathing gas during periods of recovery (marked by the prompt recovery of SpO₂), ion concentrations do not decrease, indicating the sluggish whole-body clearance of metabolic by-products following periods of extended systemic hypoxia.

Figure 5C presents electrochemical data collected from the same samples analyzed by ABG in Fig. 5B. Raw potentiometric and amperometric data are converted to ion concentrations using two-point calibrations obtained for each probe prior to measurement (calibrations performed within 2 hours of measurement). For clarity, potentiometric data are shifted based on each probe's calibration in PBS. Voltage traces obtained from K⁺ and pH sensing electrodes display minimal potentiometric drift and comparatively little noise during blood measurement. Likewise, the progressive increase in electrode potential for K⁺ and the negligible change in electrode potential for pH agree qualitatively with the changes in ion activity reported by ABG. Amperometric lactate sensing electrodes also exhibit low noise, displaying the expected Cottrellian profiles associated with a diffusion-limited electrode reaction. This, coupled with the progressive increase in reductive current ($I_{T=10s}$) following initial suffocation, suggests the stable operation of electrochemical biosensors in arterial whole blood.

The quantitative agreement between ABG analysis and electrochemical measurement is presented in Fig. 5 (D to F) for a total of six probes from two separate experiments. Figure 5 (E and F) demonstrates strong linear correlations between the concentrations of K⁺ ($R^2 = 0.83$) and lactate ($R^2 = 0.91$), determined electrochemically with those obtained from ABG. Due to the negligible changes to circulating blood pH, a similar correlation could not be established for the pH sensing electrode; however, pH values determined electrochemically agree quantitatively with those obtained by ABG within $\pm 0.1 \log_{10}([H^+])$.

Model systems for local tissue ischemia

The results presented in Fig. 5 demonstrate the stable operation of the multianalyte electrochemical platform in a physiologically relevant environment (blood). To extend this functionality to tissue, electrochemical probes were evaluated using two porcine model systems for local muscle ischemia. Porcine experimentation was conducted under general anesthesia, in the context of an Institutional Animal Care and Use Committee (IACUC)-approved nonsurvival model using Berkshire pigs (IACUC number 21-0415). The first, referred to here as the "flap model," involved the implantation of electrochemical probes into pedicled rectus abdominis myocutaneous flaps raised upon live anesthetized swine, as displayed schematically (right) and photographically (left) in Fig. 6A. Within this model, the tissue volume into which probes are introduced is completely isolated from the surrounding physiology apart from the deep superior epigastric artery/vein and the superficial superior epigastric vein, which provide necessary blood flow to maintain tissue perfusion. Occlusion of either the arterial supply or venous return (by the application of an Acland clamp) affords direct, reversible, and repeatable tissue deoxygenation to mimic the hypoxic tissue environment encountered during ACS.

In addition to the flap model, electrochemical probes are also evaluated in a live swine model of hindlimb compartment syndrome (21), to more closely mirror the physiology of human ACS. In this system, referred to here as the "compartment model," a balloon catheter is implanted between the anterior muscle compartment of the hind limb and the anterior face of the tibia (Fig. 6B). Changes to

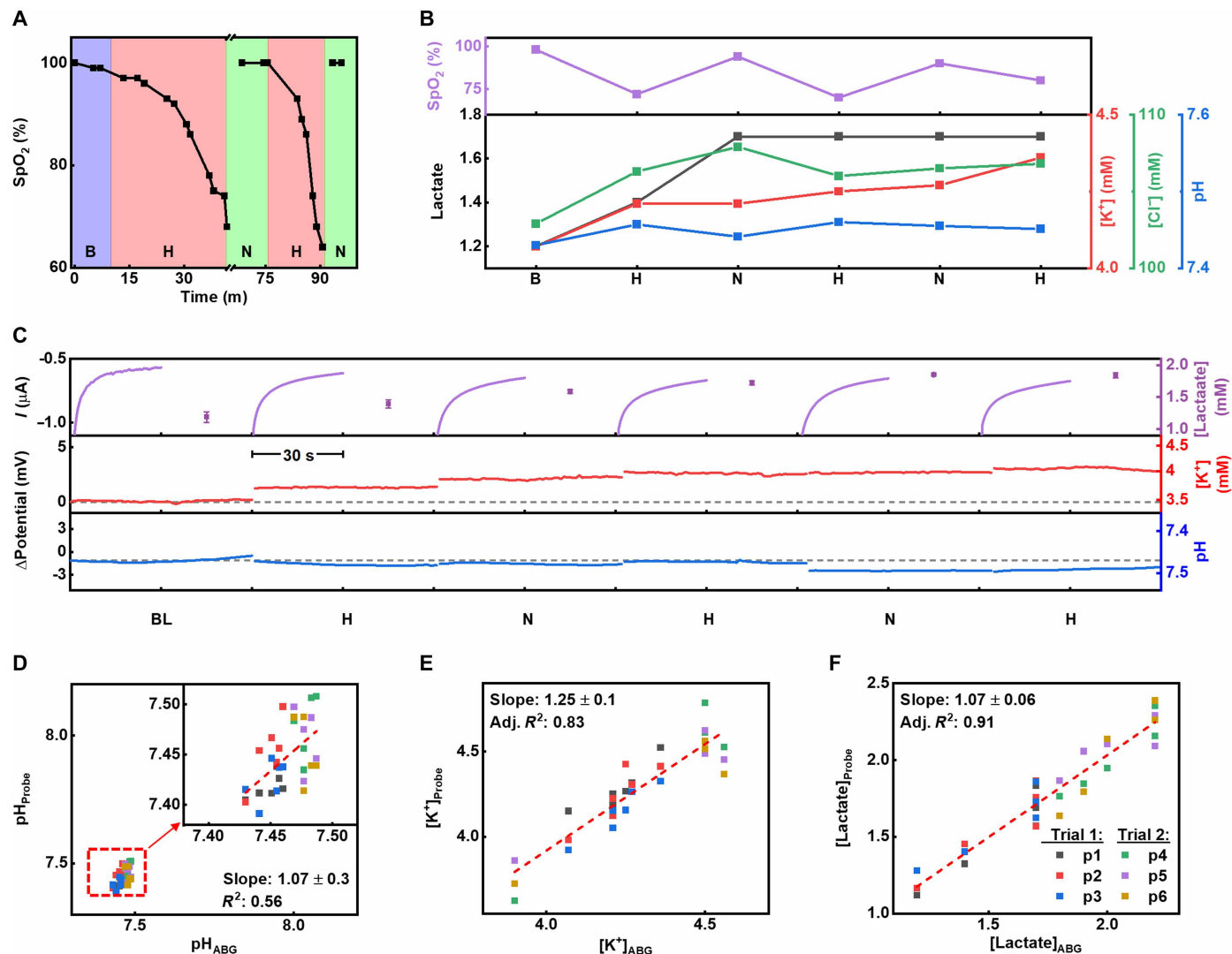


Fig. 5. Ion profiling in arterial whole blood and comparison against clinical gold standard. (A) SpO₂ profile obtained during systemic deoxygenation of a live pig to modulate circulating ion concentrations. (B) Representative ion concentrations determined by ABG analysis of samples obtained at different levels of whole-body oxygenation. (C) Raw electrochemical data obtained from lactate (top), K⁺ (middle), and pH (bottom) electrodes during alternating periods of hypoxia and normoxemia. Ground truth comparison between ABG data and electrochemical (D) pH measurements, (E) K⁺ measurements, and (F) lactate measurements obtained from $n = 3$ devices in two separate animal trials.

compartment pressure are induced by inflating or deflating the balloon with compartment pressure quantified in real-time using a transducer connected to a slit catheter placed 1 cm lateral to the tibia.

Electrochemical characteristics obtained from tissue flaps

Figure 6C presents ion profiles obtained from indwelling electrochemical probes, implanted via an intravenous catheter (implantation depth ~4 cm, defined by the length of the catheter sheath) during a single course of ischemic insult and recovery. Prior to the onset of ischemia, probes exhibit stable baseline potentials and chronoamperometric traces (Fig. 6D), reporting cation concentrations within the expected physiological range for healthy tissue (K⁺: expected = 1 to 3 mM, measured = 2 ± 0.3 mM; pH: expected = 7.4, measured = 7.3 ± 0.1). Starting anion concentrations were slightly elevated on average (lactate: expected ≈ 1 mM, measured = 3.0 ± 0.5 mM)

in raised flaps, possibly due to local trauma incurred during flap preparation and probe placement.

Dashed vertical lines demarcate the onset and termination of arterial occlusion. At the onset of arterial clamping, and for a brief time (~90 s) immediately following, little change is observed in the potentials developed by potassium and pH sensing electrodes, indicating the initial maintenance of normal metabolic function. As ischemia progresses, however, rapid and statistically significant changes in [K⁺] ($P = 2.4 \times 10^{-5}$), [H⁺] ($P = 5.6 \times 10^{-5}$), and [lactate] (8.3×10^{-6}) materialize relative to baseline as evidenced by positive potentiometric deflections obtained from cation sensing electrodes and an increase in the magnitude of reductive current developed at lactate sensing electrodes. Metabolic changes reach maxima (>5 mM K⁺, 5 to 7 mM lactate, and pH < 6.7 at peak ischemia) between 10 and 25 min postclamping, as displayed in Fig. 6G.

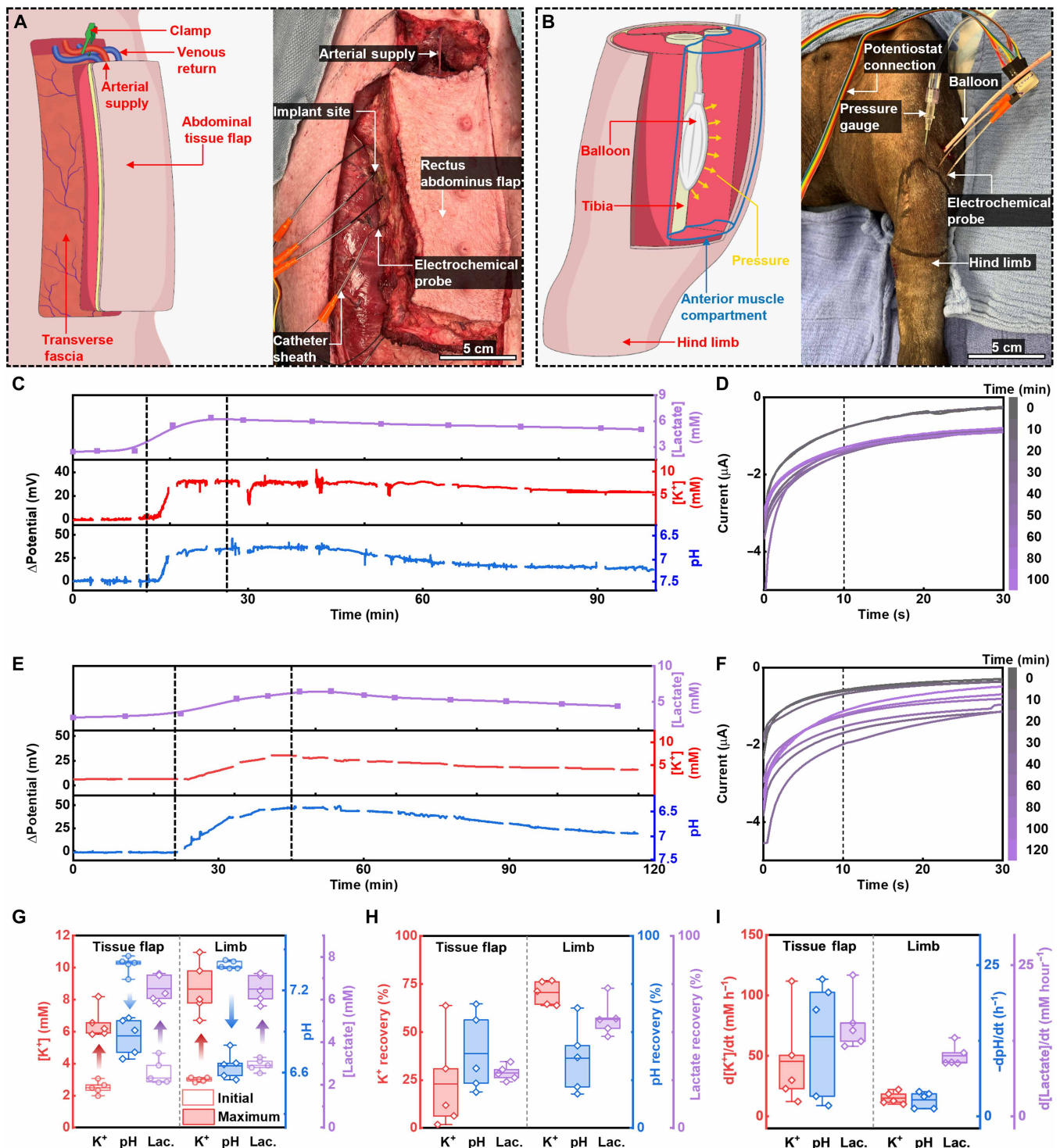


Fig. 6. In vivo ion profiling during ischemic onset in a myocutaneous flap and peripheral muscle compartment. (A) Schematic representation (left) and digital photograph (right) of tissue flap ischemia model. (B) Schematic representation (left) and digital photograph (right) of compartment ischemia model. (C) Representative electrochemical data and ion concentrations obtained from multianalyte probes implanted in a tissue flap. (D) Chronoamperometric traces used to compute lactate concentrations presented in (C). (E) Representative electrochemical data and ion concentrations obtained from multianalyte probes implanted in a muscle compartment. (F) Chronoamperometric traces used to compute lactate concentrations presented in (E). (G) Initial (hollow box) and maximum (filled box) biomarker concentrations obtained during flap (left) and limb (right) measurements. (H) Metabolic recovery 90 min post-ischemia in both the tissue flap (left) and compartment (right) models. (I) Rate of metabolic changes induced during ischemic onset in both the tissue flap (left) and compartment (right) models (total $n = 5$ devices for each physiological model; symbols, measured values; boxes, interquartile range; horizontal lines, mean values; whiskers, 5th to 95th percentiles). (A) and (B) were produced using Adobe Illustrator.

Downloaded from https://www.science.org at Northwestern University on May 27, 2026

Despite the prompt increase in metabolite concentrations, little biochemical change is observed on clamp removal despite the return of normal tissue perfusion. Even after 90 min of reperfusion without additional insult, metabolite concentrations remain elevated with only modest recovery toward baseline values (K^+ : $23 \pm 25\%$ recovery, pH: $39 \pm 20\%$ recovery, lactate: $29 \pm 4\%$ recovery; Fig. 6H). This suggests that the time frame for full biochemical recovery in this tissue model exceeds the duration of the present experiment. It could also reflect incomplete reversibility in the tissue ischemia model resulting from permanent damage to the cellular volume into which the electrochemical probes are introduced.

Electrochemical characteristics obtained from muscle compartments

Ion profiles and amperometric traces obtained from compartment-model measurements are provided in Fig. 6 (E and F), respectively. Many of the electrochemical characteristics present in the flap model are reflected in the compartment model. Both models show stable ion profiles prior to initial insult, with a significant increase in local ion concentrations following ischemic injury (pressure maintained above 120 mmHg). Despite the different methodology used to affect blood-supply occlusion, comparable ion concentrations are developed across both models (>5 mM K^+ , 5 to 9 mM lactate, and pH < 6.6 at peak ischemia; Fig. 6G). Physiological differences emerge in the rate at which these biochemical changes proceed. While results obtained from the limb model display a gradual change in biomarker concentration (progressive increases over the span of ~ 20 min), results from the flap model report much faster accumulation (full biochemical change in 5 to 10 min) in response to ischemic insult as quantified in Fig. 6I. Statistically significant differences are apparent in the first time derivative of pH (flap: -13.2 ± 9.9 pH hour $^{-1}$, limb: -2.7 ± 1.3 pH hour $^{-1}$; $P = 0.047$) and lactate (flap: 15.4 ± 4.7 mM hour $^{-1}$, limb: 10.0 ± 1.8 mM hour $^{-1}$; $P = 0.047$) signals. While differences are apparent in the onset of K^+ , the probe-to-probe variance is too great to draw statistical inference (flap: 45.4 ± 39.7 mM hour $^{-1}$, limb: 15.0 ± 5.1 mM hour $^{-1}$; $P = 0.13$). The origin of this high variance is possibly the result of heterogeneities in target tissues, as probes placed in closer proximity to supporting vasculature are expected to display differences in their temporal response. These differences are exacerbated in tissue flaps as changes occur over such a short timescale that deviations of a few minutes can strongly influence the computed rate. Notably, when the rate of change is reduced, as in the limb model, variance is similarly reduced, suggesting that the probes themselves offer reliable recording, but the physiological model may need refinement to guarantee closer agreement based on sampling depth and tissue heterogeneity. Last, differences between the two models are also apparent in the rate of biochemical recovery 90 min post-insult, with the observed recovery of K^+ and lactate from limbs (K^+ : $71 \pm 6\%$, lactate: $57 \pm 10\%$) significantly exceeding that of tissue flaps (K^+ : $23 \pm 25\%$, lactate: $29 \pm 4\%$) as presented in Fig. 6H (comparison P values $K^+ = 0.0036$, lactate = 0.0003).

To corroborate the ion concentrations determined by electrochemical measurement, a microfluidic collection catheter (fig. S11) is used to sample interstitial fluid (ISF) near (within 3 cm) the electrochemical probe implantation site for ex situ analysis. While lactate concentrations obtained with nuclear magnetic resonance spectroscopy align well with results obtained electrochemically (fig. S12), K^+ concentrations determined with inductively coupled plasma mass spectrometry (ICP-MS) display elevated values relative to those

obtained in vivo. While both the electrochemical measurement and ICP-MS data demonstrate an increase in K^+ concentration following ischemia, with K^+ increasing substantially following the onset of ischemia, the elevated starting concentration (5 to 6 mM) and very high final concentrations (~ 12 mM) obtained from ICP-MS suggest potential interference from intracellular potassium (during storage, transport, or digestion of samples) using this analytical method. The differences obtained from ex vivo lactate and K^+ measurements reflect the relative concentrations of these species in the ISF ($[K^+] \approx 3$ mM, [lactate] ≈ 1 mM) compared against their intracellular concentrations ($[K^+] \approx 150$ mM, [lactate] ≈ 3 mM depending on the cell) (44–46). Due to the high intracellular concentration of K^+ , even a small number of cells can contaminate the ISF volume, whereas this effect is expected to be far less severe for lactate. These challenges highlight the utility of an in vivo platform in characterizing tissue ion concentrations.

DISCUSSION

The multianalyte electrochemical platform described here accommodates accurate, real-time, profiling of three key biomarkers (K^+ , pH, and lactate) associated with local and systemic metabolic dysregulation. The sensing system consists of an implantable electrochemical probe interfaced with a wireless, reusable, recording/communication module transmitting real-time data to Bluetooth-enabled devices. The miniaturized electrochemical probe supports six individually addressable electrodes within a sufficiently small footprint (outer diameter < 1.4 mm) to accommodate minimally invasive probe delivery through a 14-gauge intravenous catheter. Similarly, the incorporation of an elastic nitinol support and an injection molded encapsulating sheath improve probe implantation and retention, while simultaneously preventing direct contact between sensing electrodes and target tissues, improving signal stability and longevity.

Detailed benchtop evaluation of this system in myriad liquid and semisolid media (aqueous, hydrogel, and tissue facsimile) demonstrates the selectivity and sensitivity of the electrochemical platform in accurately quantifying subtle changes to local ion concentrations. Similarly, long-term recording measurements demonstrate good agreement between the time frames for stable recording and the time frames relevant to ACS diagnosis and treatment (~ 12 hours). Furthermore, measurements in arterial whole blood validate the performance of the sensing system in physiological environments, with sensing accuracies comparable to those of a clinically relevant arterial blood-gas analyzer. Last, measurements in muscle tissue under ischemic and normoxic conditions in two different physiological models confirm the utility of the sensing platform in detecting local changes to tissue metabolism.

Notably, electrochemical probes display adequate stability and sensitivity to differentiate key physiological features from these different ischemia models. As described in Fig. 6 (H and I), the time dependence of metabolic changes differs based on model. While tissue flaps display rapid changes to local ion concentrations, muscle compartments exhibit more gradual accumulation of anaerobic biomarkers. Differences in metabolite accumulation between these two models may be due to the comparatively rapid and complete circulatory occlusion accessed in the flap model, which is not reflected in a limb compartment model. Similarly, the elimination of ancillary vasculature supporting the tissue flap may serve to reinforce the onset of deep ischemia. The restricted vascularization of the flap model also explains the slow biochemical recovery of tissue flaps when

compared with limbs, as biochemical clearance from flap tissue is completely reliant on a single vascular axis. While electrochemistry alone cannot unambiguously prove this hypothesis, it is supported by previous reports exploring the effects of ischemia on these model systems, wherein myocutaneous flaps display incomplete recovery of local StO_2 (19) while ischemic limb models display more complete recovery, following roughly equivalent bouts of local ischemia (21). Overall, this platform represents a useful technology for the determination of metabolic disruption in target tissues with potential applications in the early diagnosis of ACS and other pathologies induced by insufficiencies in local oxygen availability.

More broadly, multianalyte profiling of metabolic dysregulation in otherwise healthy tissue is critical in capturing early warning signs for the onset of local ischemia prior to irreversible tissue damage. The technology reported here offers such a measurement scheme without necessitating surgical intervention by the introduction of a minimally invasive electrochemical probe to target tissues via a delivery catheter. The multielectrode assembly offers detailed profiling of clinically relevant metabolic biomarkers in the challenging environment of deep tissue with the potential for extended recording up to 12 hours. Furthermore, the inclusion of internal calibration checking, and the rapid percutaneous introduction of probes into tissue (implantation time < 1 min) supports rapid replacement of single-use probes if an error is detected or if extended recording durations (>12 hours) prove necessary. Over longer recording durations, inflammation and infection at the implantation site may become important considerations. These factors, as well as the incorporation of this system into clinical workflows, are discussed in more detail in the supporting information.

The resolution of the sensing system aligns well with the conventional diagnostic thresholds for metabolic dysregulation. The probes presented here can confidently resolve local changes in lactate as low as 0.3 mM, supporting the early diagnosis of hyperlactemia ($[\text{lactate}] > 2$ mM) and eventually lactic acidosis ($[\text{lactate}] > 4$ mM). Probes display a similar sensitivity to K^+ , displaying a quantifiable resolution of 0.5 mM, allowing the early detection of hyperkalemia ($[\text{K}^+] > 5.5$ mM) and physiologically dangerous K^+ levels ($[\text{K}^+] > 6.5$ mM). Furthermore, as tissue acidosis involves both an increase in lactate and a decrease in pH, the probes presented in this work allow a more confident diagnosis of severe tissue acidosis by correlating data obtained from lactate and pH electrodes.

Results obtained from both benchtop and in vivo measurements demonstrate that this sensing architecture is capable of providing critical data on the health of tissues at risk of ACS due to trauma or reperfusion injury, marking the present technology as potentially important in improving surgical outcomes and reducing the costs associated with interventional fasciotomy and debridement. Furthermore, due to the sensitivity and small size of the present technology, it has the potential to provide equivalent benefit in diagnosing less severe manifestations of tissue ischemia such as chronic exertional compartment syndrome.

Beyond its utility in quantifying lactate, K^+ , and pH in vivo, the catheter-type probe and wireless recording module presented here represents a versatile electrochemical platform to profile biochemical signals in complex or inaccessible physiological environments. The assembly methods used to construct and encapsulate these sensors permits the assembly of probes of variable length (up to and exceeding 1 m), supporting biochemical detection in deep tissue. Similarly, by modifying electrode chemistries, this architecture can

be readily adapted for the detection of other biomarkers (Na^+ , Cl^- , NH_4^+ , glucose, creatine kinase, O_2 , NO, etc.) amenable to either potentiometric or amperometric sensing schemes. Last, the wireless recording platform described here represents a fully functional and reprogrammable potentiostat, whose operation can be customized to fit the needs of the measurement. This combination of structural, chemical, and measurement versatility marks the electrochemical technology disclosed here as a valuable tool for biochemical profiling in challenging physiological environments to provide critical diagnostic information supporting interventional medicine.

MATERIALS AND METHODS

Materials

Unless otherwise stated, all materials were used as received without further purification. Gold(III) chloride trihydrate ($\geq 99.9\%$), gold wire (0.5-mm diameter, 99.99%), ammonium chloride (EMSURE), sulfuric acid (95.0 to 98.0%), aniline ($\geq 99.5\%$), poly(sodium 4-styrenesulfonate) (average $M_w \sim 1,000,000$), 3,4-ethylenedioxythiophene (97%), valinomycin ($\geq 99.0\%$), potassium tetrakis(4-chlorophenyl)borate (Selectophore, $\geq 98.0\%$), bis(2-ethylhexyl) sebacate (Selectophore, $\geq 97.0\%$), poly(vinyl chloride) (Selectophore, high molecular weight), tetrahydrofuran ($\geq 99.9\%$, anhydrous), silver nitrate ($\geq 99.0\%$), sodium thiosulfate (99%), sodium hydrosulfite ($\geq 82.0\%$), potassium chloride ($\geq 99.0\%$), sodium chloride ($\geq 99.0\%$), Nafion 117 containing solution (~5 wt % solution in a mixture of lower aliphatic alcohols and water), potassium hexacyanoferrate(III) ($\geq 99.0\%$), potassium hexacyanoferrate(II) trihydrate (98.5 to 102%), iron(III) sulfate hydrate (97%), LOx (from *Aerococcus viridans*), chitosan (medium molecular weight), agarose (high electroendosmosis), and polyvinyl butyral were purchased from Sigma-Aldrich. PI films (75- μm thickness, 15.24-cm width) were purchased from Argon. Gold (99.999%) and chromium (99.95%) pellets for electron beam evaporation were obtained from Kurt J. Lesker Company. Double-sided copper clad laminate (Pyrulux, M916137) was purchased from DuPont. Stainless steel solder flux (Superior No. 71) was obtained from Superior Flux & Mfg. Co. Copper wire [44 American wire gauge (AWG)] was purchased from Remington Industries. Polyolefin heat-shrink tubing was purchased from Raychem. Nitinol wire (180- μm diameter) was obtained from Component Supply Company. Photocurable epoxy [Norland Optical Adhesive (NOA) 61] was purchased from Norland Optical; two-part fast curing (5-min) epoxy was purchased from Devcon. Polydimethylsiloxane (PDMS; Sylgard 184) was obtained from Dow Corning.

Probe head fabrication

Implantable probe heads were fabricated from Au-coated PI films via laser ablation as detailed in fig. S2. Fabrication began with electron beam deposition of metal films (100-nm Au, 20-nm Cr adhesion layer, AJA International) onto a large PI substrate (75- μm thickness, surface area ~ 700 cm^2) whose surface had been cleaned (sequential rinsing with water, isopropanol, acetone, and isopropanol) and treated with ultraviolet (UV) ozone (UVOCS; 5 min). Deposition was performed sequentially on both sides of the substrate at a constant rate of 1 $\text{\AA} \text{ s}^{-1}$. Following deposition, the substrate was cut into rectangular pieces (50 mm by 75 mm), and symmetric electrode traces were defined on both top and bottom using a UV laser micromachining system (Protolaser U4, LPKF Laser and Electronics SE) at an output power of 0.5 W in a single pass. This laser power was sufficient to affect the complete ablation of the Au/Cr layer along the cutting path

with little damage to the underlying PI (PI etching was observed to a depth of $\sim 10\ \mu\text{m}$; fig. S2C). Following electrode patterning, individual probe heads were cut from the substrate (0.5 W, 30 repetitions), which was peeled away leaving the completed sensing heads. Patterning in this fashion allowed the rapid and high yield production of electrochemical probes, with each 50 by 75 mm substrate yielding 60 probes at a total patterning time of $\sim 30\ \text{min}$.

Interconnect fabrication

Electrical connection between communication circuitry and the probe head was accomplished with a copper FPCB as detailed in Fig. 2A. FPCBs were patterned via laser etching (output power of 5.6 W, one repetition) from a double-sided copper clad laminate (Pyrulux) leveraging the same approach detailed for the probe heads. Following circuit patterning, interconnects were cleaned by bath sonication in stainless steel solder flux (Superior No. 71, SRA Soldering Products) and isopropanol (3 min each) to remove oxidized copper and carbonaceous char residues. The interconnect assembly was completed by soldering enameled Cu wires (44 AWG, Remington Industries) to the six contact pads at the base of each interconnect.

Probe assembly

Solder-less pressure connections were used to link the electrochemical probe head to the interconnect circuitry. Connections were realized using polyolefin heat-shrink tubing (Raychem, Microfit) and flexible bridging circuits as detailed in Fig. 2A. Each probe consists of one double-sided sensing head connected to the corresponding FPCB via two bridging circuits (one above and one below). Bridging circuits were fabricated from Au-coated PI using the same method as the probe head and were designed to complement the terminating traces at the proximal end of the electrode array. In a typical assembly, bridging circuits were attached on both sides of the probe head using a short ($\sim 5\ \text{mm}$) piece of heat-shrink tubing (254- μm inner diameter before shrinking). This assembly was then attached to the interconnect circuit using another piece of heat-shrink tubing (508- μm inner diameter before shrinking, 15-mm length) to form electrical contact between the FPCB and reinforce the interconnect assembly.

To improve probe stability and implantation efficacy, a nitinol wire (180- μm diameter, 130-mm length) was attached to the proximal end of the interconnect circuit using polyolefin tubing (508- μm inner diameter, 15-mm length). Connecting wires were then wrapped around the nitinol core to minimize the risk of circuit disconnect during probe deformation and to prepare the device for subsequent encapsulation. The free ends of these wires were then soldered to a Cu FPCB terminating in a male board-to-board connector (2386586-1 386587-1, TE Connectivity). Last, the circuit connections were potted with a two-part epoxy (Devcon, 5-min epoxy) to prevent water intrusion.

Electrode encapsulation

Electrochemical probes were encapsulated in a UV curable optical adhesive using the injection molding approach detailed schematically in fig. S2D. Briefly, two-part resin master molds were 3D printed (Form3B, Clear V4 resin, Formlabs) to define the size, shape, and topology of the encapsulating structure. From these master molds, self-adhesive PDMS working molds were cast (25:1 base to curing agent, cured at 70°C , 2 hours) with the dual function of containing the injected adhesive and precluding its direct contact with the electrode pads. The latter was accomplished by PDMS pillared structures,

which elastically and adhesively contacted electrode surfaces when the two sides of the mold were combined (fig. S2D).

A UV curable optical adhesive (NOA 61, Norland Products Inc., NJ, USA) was then injected into the mold at a constant rate ($500\ \mu\text{l}\ \text{min}^{-1}$) using a syringe pump (Harvard Apparatus). The filled mold was then cured under UV irradiation ($1000\ \mu\text{W}/\text{cm}^2$, Edmund Optics, 45 min), after which the two halves of the mold were separated, liberating the fully encapsulated probe tip. A similar approach was used to encapsulate the probe body, using a PDMS mold featuring a cylindrical volume to completely cover the nitinol core and connecting wires linking the probe tip to the readout circuitry.

Electrochemical apparatus

All electrochemical measurements and depositions were performed using a PalmSens4 portable potentiostat unless otherwise specified. Multielectrode tests leveraged the electrode multiplexer (MUX) add-on allowing for simultaneous measurement from eight electrodes. Electrochemical impedance spectroscopy was conducted between 1 MHz and 1 mHz at six points per decade with a sinusoidal voltage amplitude about the open-circuit voltage of 10 mV. Impedance fitting was achieved using the ZFit functionality implemented in the EC-Lab software provided by BioLogic.

Preparation of porous gold working electrodes

High-surface area gold electrodes were used to increase the current densities obtained during amperometric lactate detection. The deposition of porous gold structures was realized by electrodeposition from an aqueous solution of 10 mM $\text{AuCl}_3 \cdot 3\text{H}_2\text{O}$ and 2.5 M NH_4Cl as detailed elsewhere (47). Deposition was conducted at a constant voltage of $-0.6\ \text{V}$ versus Ag/AgCl for 60 s using a commercial Ag/AgCl reference electrode (double junction, BASi) and Au wire counter electrode. Deposition of porous gold was evidenced by a distinct color change of the working electrode from lustrous gold to a matte red color and characterized by cyclic voltammetry and scanning electron microscopy (FEI Quanta 650; fig. S13).

Preparation of pH sensing electrodes

pH sensing electrodes were prepared by potentiometric deposition of PANI from an aqueous solution of 1 M H_2SO_4 containing 0.5 M aniline monomer. Deposition was affected by cyclic voltammetry between -0.2 and $0.9\ \text{V}$ versus Ag/AgCl at a scan rate of $50\ \text{mV}\ \text{s}^{-1}$ for a total of three cycles using a commercial Ag/AgCl reference electrode and a Au wire as counter electrode (fig. S14). Following deposition, the electrode was rinsed with deionized (DI) water and voltammetrically cycled (-0.2 to $0.8\ \text{V}$ versus Ag/AgCl, $100\ \text{mV}\ \text{s}^{-1}$) for 100 cycles in 0.5 M H_2SO_4 to facilitate the complete removal of oligomeric species.

Preparation of K^+ ISEs

Potassium sensing electrodes were prepared by the application of a K^+ ISM to the surface of a PEDOT:PSS transducing electrode. PEDOT:PSS films were electrodeposited from an aqueous solution of 1 wt % NaPSS and 10 mM ethylenedioxythiophene via cyclic voltammetry between -0.2 and $1.2\ \text{V}$ versus Ag/AgCl at a scan rate of $50\ \text{mV}\ \text{s}^{-1}$ for a total of 20 cycles using a gold wire as counter electrode and a commercial Ag/AgCl reference electrode (fig. S14). Following deposition, a membrane cocktail was prepared consisting of 2 mg of valinomycin, 1 mg of potassiumtetrakis(4-chlorophenyl) borate, 131 mg of bisethylhexylsebacate, and 66 mg of PVC in 1.5 ml

of tetrahydrofuran as reported elsewhere (30, 34). The precursor solution was homogenized by sonication until all components fully dissolved (~15 min).

Prior to the application of the membrane, the PEDOT:PSS electrode was dried at 90°C for a minimum of 2 hours to reduce the impact of deleterious water accumulation between the transducing film and the ISM (48). After drying, 2 μ l of ISM solution were drop-cast onto the electrode surface and allowed to air dry for 20 min followed by baking at 70°C for a minimum of 1 hour. Last, an agarose membrane was applied to the electrode surface by drop-casting (2 μ l, 1 wt % agarose in DI water) and allowed to dry at room temperature for at least 2 hours. Prior to use, electrodes were incubated overnight in PBS (pH 7.4).

Preparation of reference electrodes

Preparation of solid-contact Ag/AgCl electrodes proceeded by the electrodeposition of metallic Ag and subsequent oxidation to AgCl. Ag was electrodeposited under a constant reducing current (50 μ A, 300 s) from an aqueous solution containing 0.25 M AgNO₃, 0.75 M Na₂S₂O₃, and 0.43 M Na₂S₂O₄ using a portable potentiostat (PalmSens4, PalmSens) with a polished Ag wire serving as counter and reference electrode as detailed elsewhere (49). The resulting Ag electrode was subsequently oxidized to AgCl by polarization to 0.2 V versus Ag/AgCl in 0.1 M KCl. The successful conversion of Ag to AgCl was evident by an obvious color change from metallic gray to dark black and the formation of isolated halide crystals at the electrode surface (fig. S14).

Due to the Nernstian Cl⁻ response of Ag/AgCl electrodes in aqueous media, a buffer membrane was necessary to standardize the chloride activity near the electrode surface. Three membrane formulations were explored to serve this purpose: a sulfonated fluoropolymer (Nafion), a PVB membrane, and an Ag/AgCl nanoparticle-loaded PVB composite. Each membrane was applied by drop-casting 2 μ l of the parent cocktail onto the Ag/AgCl contact followed by drying under flowing N₂ (~10 min) (50). A 5 wt % Nafion suspension in methanol served as the cocktail for Nafion membranes while the PVB membrane was prepared as detailed elsewhere (51). In brief, a 10 wt % stock solution of PVB was prepared in methanol via ultrasonication. To this stock solution, NaCl (10 mg/ml) was added to yield a saturated solution of Cl⁻ in the PVB matrix. This solution was then cast onto the electrode surface and allowed to dry completely.

The final formulation used the same PVB stock solution, again containing NaCl (10 mg/ml), to which AgNO₃ (10 mg/ml) was added. Mixing this solution in a vortex mixer (2000 rpm, 5 min) yielded a white colloidal suspension of AgCl. One milliliter of this suspension was then added to a clear 1.5-ml auto-sampler vial (Ks-Tek) and photoreduced by exposure to 365-nm light (1000 μ W/cm²) for 30 min. To improve the homogeneity of photoreduction, the vial was placed on a rotating stage (60 rpm) while being illuminated from one side. Reduction was evident by the conversion of the white colloidal solution to a pink suspension due to the in situ formation of AgNPs. This solution was then immediately drop-cast onto the electrode surface and allowed to dry completely. Nafion-coated electrodes were used without further modification, whereas PVB-based electrodes were incubated in PBS overnight to improve the ionic conductivity of the membrane. Reference electrodes were tested both with and without a protective agarose coating (drop-cast, 2 μ l, 1 wt % agarose in DI water; fig. S5), and all physiological studies were conducted on devices with this agarose overlayer.

Preparation of lactate sensing electrodes

The preparation of lactate sensing electrodes began with the electrodeposition of porous gold as described above followed by the deposition of Prussian blue as a selective hydrogen peroxide electrocatalyst (37). Prussian blue was electrodeposited under a constant reductive current density of 5 μ A mm⁻² for 5 min from an aqueous solution containing 20 mM K₃Fe(III)(CN)₆ and 20 mM Fe₂(III)(SO₄)₃ using a gold electrode as counter and reference (52). Following the deposition of the peroxide transducing layer, an enzyme solution was prepared by dissolving 1500 U/ml of LOx into PBS (pH 7.4). This solution was then mixed 1:1 by volume with a 1 vol % acetic acid solution containing 0.6 wt % chitosan. This solution was then drop-cast onto the Prussian blue electrode (5 μ l) and dried overnight at 35°C (53). Last, an agarose membrane was applied to the electrode surface by drop-casting (2 μ l, 1 wt % agarose in DI water) and allowed to dry at room temperature for at least 2 hours.

Sensor calibration

Potentiometric and amperometric ion sensors were calibrated in several liquid and solid environments to mimic the physiological conditions encountered in living tissue. Baseline calibrations were conducted in aqueous solutions containing 0.1 M NaCl as background. For K⁺ sensor calibration, the total ionic strength of the solution was fixed at 0.1 M, adjusting the background NaCl concentration accordingly (apart from the 1 M KCl measurement whose ionic strength was 1 M). pH calibration proceeded from a starting pH of 5 (by addition of HCl) titrating with NaOH to realize a progressively more basic environment. A commercial pH meter (Mettler Toledo FP20) was used to verify the target pH of the solution prior to measurement. Lactate calibration proceeded in PBS solution by the addition of sodium lactate. For each measurement, probes were given a 10-s equilibration time when introduced into new solution prior to the start of measurement. In addition to 0.1 M NaCl, a protein-rich environment was also investigated by the addition of 0.5 wt % BSA to evaluate any putative effects from protein biofouling during short-term recording.

Validation in agarose gel

The performance of electrochemical probes in semisolid material was evaluated using agarose hydrogel. Gels were fabricated as follows: 0.2 g of agarose powder was added to 20 ml of 0.1 M NaCl and microwaved at 30-s intervals until the powder fully dissolved. This parent solution was allowed to cool to room temperature, at which point requisite amounts of KCl, sodium lactate, or HCl/NaOH were added to generate analogous standard concentrations to those reported in preceding section. Solutions were then allowed to cool at 4°C until the gel solidified. Probes were evaluated by implantation into these gel samples following a 30-s equilibration time.

Validation in tissue facsimile

A tissue facsimile was used to evaluate the performance of electrochemical probes in a similar mechanical environment to living muscle. To this end, rectangular slabs (5 cm by 1 cm by 1 cm, length by width by height) of pork loin were cut, rinsed aggressively with DI water and soaked in calibration solutions (identical to those described in preceding sections) for 15 min. Following this soaking time, slabs were dabbed dry with an absorptive cloth before introducing the electrochemical probe. Probes were placed between two identical slabs with electrodes facing the upper and lower surfaces of

the tissue. Between each measurement, probes were rinsed with DI water. Probes were allowed a 30-s equilibration time prior to the start of potentiometric or amperometric calibration.

Finite element simulation

Finite element simulations considering enzymatic activity and electrocatalytic consumption of peroxide were performed using MATLAB to elucidate H_2O_2 and lactate concentrations near the electrode surface both at rest and during active polarization (fig. S7C). The simulation cell for these simulations consisted of a 30 mm by 3 mm by 3 mm (length by width by height) volume using the designed geometry of the electrochemical probe. This volume was discretized homogeneously with a grid spacing of 0.05 mm, yielding a total voxel volume of $1.25 \times 10^{-4} \text{ mm}^3$. The model assumes Fickian diffusive transport of all chemical species, ignoring any contribution from solution convection. Michaelis-Menten kinetics are assumed for LOx with a Menten coefficient of 2.6 mM with a maximum velocity of 0.001 M s^{-1} (41). Diffusion coefficients for lactate and H_2O_2 were 9.63×10^{-4} and $1.9 \times 10^{-3} \text{ cm}^2 \text{ s}^{-1}$, respectively (54, 55). Concentration gradients were computed every 0.1 s with steady-state ion gradients obtained by allowing the system to equilibrate for 900 s. During periods of reductive polarization, perfect electrocatalytic consumption of H_2O_2 is assumed, such that $[\text{H}_2\text{O}_2]$ at the electrode surface remains 0 mM. Simulated chronoamperograms are obtained from peroxide flux at the electrode interface assuming the two-electron reduction of peroxide to water at the Prussian blue surface. Additional simulation details are provided in the Supplementary Materials.

Probe validation in arterial whole blood

Initial physiological validation of electrochemical probes was conducted in arterial whole blood collected from anesthetized pigs during periods of normal oxygenation and induces suffocation. All animal experiments presented here were conducted in a nonsurvival model using Berkshire pigs with the approval of the IACUC (number 21-0415) at Washington University School of Medicine. This was performed as per US Department of Agriculture Animal Welfare Regulations at an accredited facility. In this study, two swine were used in separate experiments. Anesthesia was induced with Telazol, ketamine, and xylazine followed by maintenance with isoflurane. At the end of the experiment, each animal was euthanized with pentobarbital.

Circulating ion concentrations were modulated by progressive suffocation of sedated animals by N_2 enrichment of the breathing gas. Undiluted whole blood samples were collected in heparinized syringes (1 ml, EXEL, USA) from an arterial line during periods of normal oxygenation and induced hypoxia. Immediately following collection (within ~2 min), blood samples were characterized with a critical care blood gas analyzer (Stat Profile Prime+, Nova Biomedical) and with electrochemical probes to directly compare the performance of the implantable electrochemical platform with a clinical standard.

Probe validation in myocutaneous tissue flaps

Probe validation in living muscle was performed by implantation into free-standing abdominal tissue flaps. Briefly, pedicled rectus abdominis myocutaneous flaps were raised based upon the deep superior epigastric artery and veins in addition to the superficial superior epigastric vein (19). Individual probes were delivered into abdominal muscle tissue with an intravenous catheter (14-gauge, King Way Beauty Manufacturer, USA) to an approximate implantation depth of

~6 cm. Multiple probes were deployed in each flap with a lateral separation of ~3 cm to provide replicate electrochemical measurement of the tissue volume. Probe deployment was completed within ~30 s of catheter insertion.

Following flap creation and probe implantation, probes were allowed to equilibrate (while recording) for a minimum of 20 min to obtain stable baseline signal prior to ischemic insult. Ischemia was introduced by clamping the deep superior epigastric artery with an Acland clamp. Blood supply occlusion was maintained for at least 15 min before the clamp was removed, returning normal perfusion to the tissue volume. Tissue flaps were allowed to recover for at least 90 min following ischemic insult. Throughout this sequence of trauma and recovery, potentiometric data from K^+ and pH sensing electrodes were collected, continuously pausing only during lactate quantification. Chronoamperometric lactate quantification was conducted at intervals of 300 s during baseline collection and deoxygenation, and intervals of 600 s during recovery (the total duration of each measurement was 90 s).

Probe validation in a peripheral muscle compartment

Electrochemical probes were further evaluated in a more realistic physiological model for ACS. In this model, control over compartment pressure is realized by the insertion of a balloon catheter between the anterior muscle compartment of the animal's hind limb and the anterior face of the tibia (Fig. 6D) as described elsewhere. Changes in compartment pressure are monitored using a pressure transducer connected to a slit catheter placed 1 cm lateral to the tibia. Electrochemical probes were introduced into the anterior muscle compartment using the same method described with the flap model and allowed to equilibrate for a minimum of 20 min prior to ischemic insult. Following this baseline measurement, saline was injected into the balloon catheter to rapidly (within ~2 min) increase compartment pressure to a target range of 120 to 150 mmHg. Compartment pressure was held above 120 mmHg for 20 min, injecting additional saline whenever necessary to maintain target pressure. Following this 20-min hold, the balloon was deflated, and the tissue was allowed to recover for at least 90 min.

Implanted collection catheter

A microfluidic collection catheter was assembled to affect the recovery of ISF from target muscle tissues to validate the results obtained from implantable electrochemical probes. The catheter consisted of a nitinol frame supporting microfluidic tubing (50- μm inner diameter, PEEK, Element, Scotland) whose distal end had been perforated with regularly spaced holes (pitch: 1 mm) to improve collection yield. Microfluidic tubing was connected to a Luer lock syringe to provide mild negative pressure to encourage liquid transport into the collection area. A pressure release valve was also included to more effectively draw liquid through the microfluidic structure. A detailed description of this apparatus is provided in fig. S11.

Electronics module

The electronics enabling wireless, real time, three-electrode based electrochemical sensing of up to four distinct analytes were housed onboard a compact ($30 \times 60 \text{ mm}^2$) rigid PCB (PCBWay). The main body was interfaced to the probe's electrochemically active electrodes via an intermediary PCB with complimentary board-to-board connectors (2386586-1 386587-1, TE Connectivity), ensuring reusability, facile calibration, and probe replacement. The device itself was

powered by a small 85 mAh 3.7 V Li-Po battery (CDE, RJD2032C-1ST1), which can be recharged through a 5-V micro-USB connector and an on-board recharging integrated chip (IC) (Texas Instruments, BQ25100YFPR). The battery voltage was conditioned to 3.3 V via a high-efficiency buck-boost converter (Richtek, RT6154B) and used to power the digital supply pins of the microcontroller (MCU) and AFE IC. Moreover, the sensitive analog voltage supply was formed from the 3.3-V rail by cascading a low-pass LC filter and a high-power supply rejection ratio, precision, 2.8-V low drop-out regulator (Onsemi, NCP161AMX280TBG). This low noise rail sourced the analog domain of the AFE IC, the switch MUX matrix, and buffering op-amps. A complete circuit diagram for the recording module is provided in fig. S15.

The MCU (RP2350), supported as part of a Raspberry Pi Pico W control board, was programmed to extract real-time data through SPI communication with the low power precision AFE IC (Analog Devices, AD5941). The AD5941's integrated potentiostat, transimpedance amplifier (TIA), analog MUX, programmable gain amplifier (PGA), general purpose input output pins (GPIOs), and 16-bit successive approximation register ADC functioned as the core stimulating, conditioning, and sensing units of the electrochemical cell and combined to enable three different modes of operation. First, in potentiometric mode, the reference electrode was biased from an internal 1.1-V supply, and the potential difference between a given working electrode (K^+ , pH, second reference, or lactate) and the reference electrode was dynamically routed through the integrated MUX and conditioned by the PGA and ADC. Second, in amperometric mode, the potentiostat applied an offset bias of -0.2 V to the working electrode (lactate only) with respect to the reference electrode while the counter electrode was used to sink the induced electrochemical current. This current was subsequently measured using the AD5941's internal TIA. Last, in pulsed amperometric mode, the AFE's GPIOs controlled a high input impedance switch matrix (Texas Instruments, TMUX1112RSVR) to form electrical connections to the lactate and counter electrodes. This enabled sequential switching between amperometric and potentiometric modes, while ensuring that the counter electrode and lactate electrodes retained high impedance if unused. Moreover, all four potentiometric working electrodes were maintained in a voltage follower configuration using low noise and ultrahigh input impedance op-amps (Analog Devices, MAX40024) to reduce parasitic current leakage at the sensitive biointerfaced electrodes.

Through a custom communication application (implemented in MATLAB), incoming sensor data were streamed, and user-specified commands were received and transmitted via BLE 5.1 using the Pico's on-board wireless transmission chipset (CYW43439). A balance between low power consumption and low noise was achieved by selecting an appropriate sampling frequency (10 Hz), performing oversampling followed by decimation, and then signal averaging ($n = 10$) to achieve an effective 1-Hz measurement and refresh rate. Additional details on this measurement and communication protocol are provided in figs. S16 and S17. The wearability and practicality of the recording module, as well as its robustness against patient movement and minor impacts were also considered and are described fully in fig. S18.

While the sampling protocol described above can only realize semicontinuous amperometric profiling, the much greater stability of lactate electrodes when operated in a pulsed mode supersedes the benefits associated with continuous measurement. Furthermore, the

current lactate polling rate (one measurement every 10 min) is more than sufficient to meet the demands of clinical diagnostics. Should more frequent or on-demand measurements be necessary, additional functionality has been realized in the form of a single-point instantaneous lactate measurement implemented in software and firmware as presented in fig. S17. At the discretion of the operator, this functionality switches the recording apparatus into amperometric polling to obtain a single lactate measurement whenever desired. Should truly simultaneous measurement become necessary, the addition of a dedicated ADC handling potentiometric signals would accommodate the simultaneous collection of both potentiometric and amperometric data.

Supplementary Materials

This PDF file includes:

Supplementary Text

Figs. S1 to S18

References

REFERENCES

1. G. L. Semenza, Series introduction: Tissue ischemia: Pathophysiology and therapeutics. *J. Clin. Invest.* **106**, 613–614 (2000).
2. B. C. V. Campbell, D. A. De Silva, M. R. Macleod, S. B. Coutts, L. H. Schwamm, S. M. Davis, G. A. Donnan, Ischaemic stroke. *Nat. Rev. Dis. Primers* **5**, 70 (2019).
3. M. Gunata, H. Parlakpınar, A review of myocardial ischaemia/reperfusion injury: Pathophysiology, experimental models, biomarkers, genetics and pharmacological treatment. *Cell Biochem. Funct.* **39**, 190–217 (2021).
4. K. Gnanapandithan, P. Feuerstadt, Review article: Mesenteric ischemia. *Curr. Gastroenterol. Rep.* **22**, 17 (2020).
5. R. Berchiolli, G. Bertagna, D. Adami, F. Canovaro, L. Torri, N. Troisi, Chronic limb-threatening ischemia and the need for revascularization. *J. Clin. Med.* **12**, 2682 (2023).
6. A. G. Via, F. Oliva, M. Spoliti, N. Maffulli, Acute compartment syndrome. *Muscles Ligaments Tendons J* **5**, 18–22 (2015).
7. A. L. Davidson, M. A. Sutherland, R. C. Siska, J. E. Janis, Practical review on the contemporary diagnosis and management of compartment syndrome. *Plast. Reconstr. Surg. Glob. Open* **12**, e5637 (2024).
8. A. G. von Keudell, M. J. Weaver, P. T. Appleton, D. S. Bae, G. S. M. Dyer, M. Heng, J. B. Jupiter, M. S. Vrahas, Diagnosis and treatment of acute extremity compartment syndrome. *Lancet* **386**, 1299–1310 (2015).
9. A. H. Schmidt, Acute compartment syndrome. *Injury* **48**, S22–S25 (2017).
10. N. McLaughlin, H. Heard, S. Kelham, Acute and chronic compartment syndromes: Know when to act fast. *JAAPOA* **27**, 23–26 (2014).
11. T. Bhattacharyya, M. S. Vrahas, The medical-legal aspects of compartment syndrome. *J. Bone Joint Surg. Am.* **86**, 864–868 (2004).
12. A. H. Schmidt, Acute compartment syndrome. *Orthop. Clin. North Am.* **47**, 517–525 (2016).
13. A. M. Crespo, A. Manoli III, S. R. Konda, K. A. Egol, Development of compartment syndrome negatively impacts length of stay and cost after tibia fracture. *J. Orthop. Trauma* **29**, 312–315 (2015).
14. D. Kakagia, E. J. Karadimas, G. Drosos, A. Ververidis, G. Trypsiannis, D. Verettas, Wound closure of leg fasciotomy: Comparison of vacuum-assisted closure versus shoelace technique. A randomised study. *Injury* **45**, 890–893 (2014).
15. P. Mitas, M. Vejrazka, J. Hruby, R. Spunda, O. Pecha, J. Lindner, M. Spacek, Prediction of compartment syndrome based on analysis of biochemical parameters. *Ann. Vasc. Surg.* **28**, 170–177 (2014).
16. R. V. O'Toole, A. Whitney, N. Merchant, E. Hui, J. Higgins, T. T. Kim, C. Sagebien, Variation in diagnosis of compartment syndrome by surgeons treating tibial shaft fractures. *J. Trauma Acute Care Surg.* **67**, 735–741 (2009).
17. J. Montreuil, J. Corban, R. Reindl, E. J. Harvey, M. Bernstein, Novel digital continuous sensor for monitoring of compartment pressure: A case report. *OTA Int.* **5**, e208 (2022).
18. A. D. Duckworth, M. M. McQueen, Continuous intracompartmental pressure monitoring for acute compartment syndrome. *JBJS Essent. Surg. Tech.* **3**, e13 (2013).
19. D. Lu, S. Li, Q. Yang, H. M. Arafa, Y. Xu, Y. Yan, D. Ostojich, W. Bai, H. Guo, C. Wu, S. Li, L. Jacobson, A. M. Westman, M. R. MacEwan, Y. Huang, M. Pet, J. A. Rogers, Implantable, wireless, self-fixing thermal sensors for continuous measurements of microvascular blood flow in flaps and organ grafts. *Biosens. Bioelectron.* **206**, 114145 (2022).
20. D. Lu, W. Moritz, H. M. Arafa, Q. Yang, L. Jacobson, D. Ostojich, W. Bai, H. Guo, C. Wu, S. Li, S. Li, Y. Huang, Y. Xu, Y. Yan, A. M. Westman, M. R. MacEwan, J. A. Rogers, M. A. Pet,

- Intramuscular microvascular flow sensing for flap monitoring in a porcine model of arterial and venous occlusion. *J. Reconstr. Microsurg.* **39**, 231–237 (2023).
21. A. M. Westman, H. Guo, Y. Xu, W. Bai, Y. Liu, W. Ouyang, W. Moritz, L. Jacobson, Y. Weng, H. Zang, C. Wu, Z. Hu, S. Li, D. Lu, H. M. Arafa, M. R. MacEwan, L. Tatman, J. A. Rogers, M. A. Pet, Percutaneously introduced wireless intramuscular near-infrared spectroscopy device detects muscle oxygenation changes in porcine model of lower extremity compartment syndrome. *J. Orthop. Res.* **41**, 54–62 (2023).
 22. A. Agarwal, A. Gural, M. Monge, D. Adalian, S. Chen, A. Scherer, A. Emami, in *2017 Symposium on VLSI Circuits* (2017), pp. C108–C109.
 23. D. A. Baker, D. A. Gough, A. Continuous, Implantable lactate sensor. *Anal. Chem.* **67**, 1536–1540 (1995).
 24. N. P. Sardesai, M. Ganesana, A. Karimi, J. C. Leiter, S. Andreescu, Platinum-doped ceria based biosensor for in vitro and in vivo monitoring of lactate during hypoxia. *Anal. Chem.* **87**, 2996–3003 (2015).
 25. I. Watanabe, S. G. Leonard, Continuous coronary venous K⁺ monitoring during myocardial ischemia in swine hearts. *J. Nihon Univ. Med. Assoc.* **76**, 59–67 (2017).
 26. J. L. Hill, L. S. Gettes, Effect of acute coronary artery occlusion on local myocardial extracellular K⁺ activity in swine. *Circulation* **61**, 768–778 (1980).
 27. J. R. K. Marland, M. E. Gray, C. Dunare, E. O. Blair, A. Tsiamis, P. Sullivan, E. González-Fernández, S. N. Greenhalgh, R. Gregson, R. E. Clutton, M. M. Parys, A. Dyson, M. Singer, I. H. Kunkler, M. A. Potter, S. Mitra, J. G. Terry, S. Smith, A. R. Mount, I. Underwood, A. J. Walton, D. J. Argyle, A. F. Murray, Real-time measurement of tumour hypoxia using an implantable microfabricated oxygen sensor. *Sens. Bio-Sens. Res.* **30**, 100375 (2020).
 28. S. Dulay, L. Rivas, L. Pla, S. Berdún, E. Eixarch, E. Gratacós, M. Illa, M. Mir, J. Samitier, Fetal ischemia monitoring with in vivo implanted electrochemical multiparametric microsensors. *J. Biol. Eng.* **15**, 28 (2021).
 29. C. Espadas-Torre, M. Telting-Diaz, M. Meyerhoff, Electrochemical sensors for the continuous monitoring of blood gases and electrolytes. *Electrochem. Soc. Interface* **4**, 41–46 (1995).
 30. V. V. Cosofret, M. Erdosy, T. A. Johnson, R. P. Buck, R. B. Ash, M. R. Neuman, Microfabricated sensor arrays sensitive to pH and K⁺ for ionic distribution measurements in the beating heart. *Anal. Chem.* **67**, 1647–1653 (1995).
 31. S. Dulay, L. Rivas, S. Miserere, L. Pla, S. Berdún, J. Parra, E. Eixarch, E. Gratacós, M. Illa, M. Mir, J. Samitier, In vivo monitoring with micro-implantable hypoxia sensor based on tissue acidosis. *Talanta* **226**, 122045 (2021).
 32. H. T. Banks, S. Hu, Z. R. Kenz, A brief review of elasticity and viscoelasticity for solids. *Adv. Appl. Math. MEch.* **3**, 1–51 (2011).
 33. H. Fallahi, F. Taheri-Behrooz, A. Asadi, Nonlinear mechanical response of polymer matrix composites: A review. *Polym. Rev.* **60**, 42–85 (2020).
 34. Y. K. Lee, K.-I. Jang, Y. Ma, A. Koh, H. Chen, H. N. Jung, Y. Kim, J. W. Kwak, L. Wang, Y. Xue, Y. Yang, W. Tian, Y. Jiang, Y. Zhang, X. Feng, Y. Huang, J. A. Rogers, Chemical sensing systems that utilize soft electronics on thin elastomeric substrates with open cellular designs. *Adv. Funct. Mater.* **27**, 1605476 (2017).
 35. A. J. Bard, L. R. Faulkner, H. S. White, *Electrochemical Methods: Fundamentals and Applications*. (John Wiley & Sons, 2022).
 36. R. Garjonyte, Y. Yigzaw, R. Meskys, A. Malinauskas, L. Gorton, Prussian blue- and lactate oxidase-based amperometric biosensor for lactic acid. *Sens. Actuators B* **79**, 33–38 (2001).
 37. A. A. Karyakin, E. E. Karyakina, L. Gorton, On the mechanism of H₂O₂ reduction at Prussian blue modified electrodes. *Electrochem. Commun.* **1**, 78–82 (1999).
 38. N. A. Sitenkova, M. A. Komkova, I. V. Khomyakova, E. E. Karyakina, A. A. Karyakin, Transition metal hexacyanoferrates in electrocatalysis of H₂O₂ reduction: An exclusive property of prussian blue. *Anal. Chem.* **86**, 4131–4134 (2014).
 39. A. A. Karyakin, Prussian blue and its analogues: Electrochemistry and analytical applications. *Electroanalysis* **13**, 813–819 (2001).
 40. J.-M. Noël, J. Médard, C. Combellas, F. Kanoufi, Prussian blue degradation during hydrogen peroxide reduction: A scanning electrochemical microscopy study on the role of the hydroxide ion and hydroxyl radical. *ChemElectroChem* **3**, 1178–1184 (2016).
 41. I. A. Ges, F. Baudenbacher, Enzyme-coated microelectrodes to monitor lactate production in a nanoliter microfluidic cell culture device. *Biosens. Bioelectron.* **26**, 828–833 (2010).
 42. D. J. Marcinek, M. J. Kushmerick, K. E. Conley, Lactic acidosis in vivo: testing the link between lactate generation and H⁺ accumulation in ischemic mouse muscle. *J. Appl. Physiol.* **108**, 1479–1486 (2010).
 43. L. A. Shimoda, J. Polak, Hypoxia. 4. Hypoxia and ion channel function. *Am. J. Physiol. Cell Physiol.* **300**, C951–C967 (2011).
 44. M. Zaccchia, M. L. Abategiovanni, S. Stratigis, G. Capasso, Potassium: From physiology to clinical implications. *Kidney Dis. (Basel)* **7**, 72–79 (2016).
 45. D. A. MacLean, J. Bangsbo, B. Saltin, Muscle interstitial glucose and lactate levels during dynamic exercise in humans determined by microdialysis. *J. Appl. Physiol.* **87**, 1483–1490 (1999).
 46. S. Walenta, S. Snyder, Z. A. Haroon, R. D. Braun, K. Amin, D. Brizel, W. Mueller-Klieser, B. Chance, M. W. Dewhirst, Tissue gradients of energy metabolites mirror oxygen tension gradients in a rat mammary carcinoma model. *Int. J. Radiat. Oncol. Biol. Phys.* **51**, 840–848 (2001).
 47. G. Sanzó, I. Taurino, R. Antiochia, L. Gorton, G. Favero, F. Mazzei, G. De Micheli, S. Carrara, Bubble electrodeposition of gold porous nanocores for the enzymatic and non-enzymatic detection of glucose. *Bioelectrochemistry* **112**, 125–131 (2016).
 48. J. Hu, A. Stein, P. Bühlmann, Rational design of all-solid-state ion-selective electrodes and reference electrodes. *TrAC Trends Anal. Chem.* **76**, 102–114 (2016).
 49. Y. Song, J. Min, Y. Yu, H. Wang, Y. Yang, H. Zhang, W. Gao, Wireless battery-free wearable sweat sensor powered by human motion. *Sci. Adv.* **6**, eaay9844 (2020).
 50. P. Hashemi, P. L. Walsh, T. S. Guillot, J. Gras-Najjar, P. Takmakov, F. T. Crews, R. M. Wightman, Chronically implanted, nafion-coated Ag/AgCl reference electrodes for neurochemical applications. *ACS Chem. Neurosci.* **2**, 658–666 (2011).
 51. T. Guinovart, G. A. Crespo, F. X. Rius, F. J. Andrade, A reference electrode based on polyvinyl butyral (PVB) polymer for decentralized chemical measurements. *Anal. Chim. Acta* **821**, 72–80 (2014).
 52. M. Qiu, F. Zhou, P. Sun, X. Chen, C. Zhao, W. Mai, Unveiling the electrochromic mechanism of Prussian Blue by electronic transition analysis. *Nano Energy* **78**, 105148 (2020).
 53. M. E. Payne, A. Zamarayeva, V. I. Pister, N. A. D. Yamamoto, A. C. Arias, Printed, flexible lactate sensors: Design considerations before performing on-body measurements. *Sci. Rep.* **9**, 13720 (2019).
 54. A. C. F. Ribeiro, V. M. M. Lobo, D. G. Leais, J. J. S. Natividade, L. P. Veríssimo, M. C. F. Barros, A. M. T. D. P. V. Cabral, Binary diffusion coefficients for aqueous solutions of lactic acid. *J. Solution Chem.* **34**, 1009–1016 (2005).
 55. N. S. Georgescu, D. A. Scherson, Communication—Hydrogen peroxide reduction in aqueous electrolytes: Influence of a heterogeneous decomposition step. *J. Electrochem. Soc.* **163**, H630–H632 (2016).
 56. R. N. Vyas, K. Li, B. Wang, Modifying randles circuit for analysis of polyoxometalate layer-by-layer films. *J. Phys. Chem. B* **114**, 15818–15824 (2010).
 57. D. T. Miles, Run-D.M.C.: A mnemonic aid for explaining mass transfer in electrochemical systems. *J. Chem. Educ.* **90**, 1649–1653 (2013).
 58. J. C. Myland, K. B. Oldham, Cottrell's equation revisited: An intuitive, but unreliable, novel approach to the tracking of electrochemical diffusion. *Electrochem. Commun.* **6**, 344–350 (2004).
 59. J. Zhang, S. Bhattacharyya, R. C. Hickner, A. R. Light, C. J. Lambert, B. K. Gale, O. Fiehn, S. H. Adams, Skeletal muscle interstitial fluid metabolomics at rest and associated with an exercise bout: Application in rats and humans. *Am. J. Physiol. Endocrinol. Metab.* **316**, E43–E53 (2019).
 60. V. L. Clark, J. A. Kruse, Clinical methods: The history, physical, and laboratory examinations. *JAMA* **264**, 2808–2809 (1990).
 61. H. M. Thompson, D. J. Lim, C. Banks, J. W. Grayson, S. Ayinala, D. Y. Cho, B. A. Woodworth, Antibiotic eluting sinus stents. *Laryngoscope Investig. Otolaryngol.* **5**, 598–607 (2020).
 62. M. A. Halanski, M. R. Morris, B. Lee Harper, C. Doro, Intracompartmental pressure monitoring using a handheld pressure monitoring system. *JBJS Essent. Surg. Tech.* **5**, e6 (2015).
 63. A. M. Torlincasi, R. A. Lopez, M. Waseem, Acute compartment syndrome, in *StatPearls* (StatPearls Publishing, 2023).

Acknowledgments: This work was supported by the Querrey-Simpson Institute for Bioelectronics at Northwestern University. K.E.M. acknowledges support from an NIH sleep and circadian training grant (T32HL007909). J.L.C. acknowledges support from the National Science Foundation Graduate Research Fellowship under grant no. DGE-2234667. This work made use of the EPIC facility of Northwestern University's NUANCE Center, which has received support from the Soft and Hybrid Nanotechnology Experimental (SHyNE) Resource (NSF ECCS-2025633), the IIN, and Northwestern's MRSEC program (NSF DMR-2308691). This work also made use of the IMSERC (RRID:SCR_017874) NMR facility at Northwestern University, which has received support from the SHyNE Resource (NSF ECCS-2025633), Int. Institute of Nanotechnology, and Northwestern University. We thank the Baylor University Makerspace (Experiential Learning, University Libraries, Waco, TX) for the use of their 3D printing tools and resources. **Funding:** This work was supported by the Querrey Simpson Institute for Bioelectronics (D.H., E.A.O., J.G.R., S.S., S.C., and Y.-T.H.), National Institute of Health grant T32HL007909 (K.E.M.), and National Science Foundation grant DGE-2234667 (J.L.C.).

Author contributions: Conceptualization: K.E.M., R.G.N., M.A.P., and J.A.R. Methodology: K.E.M., D.H., E.A.O., S.C., R.G.N., and M.A.P. Investigation: K.E.M., D.H., E.A.O., J.G.R., S.S., S.C., J.L.C., Y.-T.H., A.M.W., and M.A.P. Visualization: K.E.M. Funding acquisition: M.A.P. and J.A.R. Project administration: R.G.N., M.A.P., and J.A.R. Supervision: R.G.N., M.A.P., and J.A.R. Writing—original draft: K.E.M. and R.G.N. Writing—review and editing: K.E.M., R.G.N., M.A.P., and J.A.R. Resources: M.A.P. and J.A.R. Data curation: K.E.M. and M.A.P. Validation: K.E.M. and R.G.N. Formal analysis: K.E.M. Software: K.E.M. **Competing interests:** K.E.M., D.H., M.A.P., and J.A.R. are listed as co-inventors on a submitted provisional patent application (021476/US Devices, Systems, and Methods for Continuous Deep Tissue Metabolic Monitoring, submitted 29 September 2025) describing the present technology. M.A.P. receives patent royalties and consulting fees from Vioptix Inc. for work unrelated to that presented in this manuscript. The other authors declare that they have no competing interests. **Data, code, and materials availability:** All data and code needed to evaluate and reproduce the results in the paper are present in the paper

and/or the Supplementary Materials. This study did not generate new materials. Custom software and firmware for the miniaturized potentiostat platform, as well as code used to simulate the electrochemical behavior of lactate electrodes, are freely available at https://github.com/kmadsen2/Miniature_ion_probe and <https://doi.org/10.5281/zenodo.17282685>.

Submitted 20 June 2025
Accepted 20 April 2026
Published 27 May 2026
10.1126/sciadv.adz8930

A miniaturized implantable electrochemical platform for continuous monitoring of metabolites in deep tissue

Kenneth E. Madsen, Dane Hintermueller, Elliot A. Opel, Joseph G. Ribaldo, Sara Saffari, Soongwon Cho, Joanna L. Ciatti, Yu-Ting Huang, Amanda M. Westman, Ralph G. Nuzzo, Mitchell A. Pet, and John A. Rogers

Sci. Adv. **12** (22), eadz8930. DOI: 10.1126/sciadv.adz8930

View the article online

<https://www.science.org/doi/10.1126/sciadv.adz8930>

Permissions

<https://www.science.org/help/reprints-and-permissions>

Use of this article is subject to the [Terms of service](#)

Science Advances (ISSN 2375-2548) is published by the American Association for the Advancement of Science. 1200 New York Avenue NW, Washington, DC 20005. The title *Science Advances* is a registered trademark of AAAS.

Copyright © 2026 The Authors, some rights reserved; exclusive licensee American Association for the Advancement of Science. No claim to original U.S. Government Works. Distributed under a Creative Commons Attribution NonCommercial License 4.0 (CC BY-NC).